

HELSINKI INSTITUTE OF PHYSICS

INTERNAL REPORT

HIP – 1998 – 01

Search for New Physics in the Lepton
Sector of the Standard Model at LEP1

Kenneth Österberg

Department of Physics, University of Helsinki
and
Helsinki Institute of Physics, Finland

ACADEMIC DISSERTATION

*To be presented, with the permission of the Faculty of Science
of the University of Helsinki, for public criticism in Auditorium XIV
on February 21th, 1998, at 10 o'clock.*

Helsinki 1998

ISBN 951-45-7961-5
ISSN 1455-0563
Helsinki University Press 1998

Preface

This thesis is based on the research work carried out during 1990-1997 as a member of the DELPHI collaboration at the Research Institute for High Energy Physics (SEFT), University of Helsinki, Finland and at CERN, the European Laboratory for Particle Physics, Geneva, Switzerland.

During these years I have received encouragement and support from many people. I would like to thank Doc. Risto Orava, my supervisor, for giving me the opportunity to work in his group and that he has since then continuously supported my activities. His encouragement and his guidance have been very valuable. I am greatly indebted to Marco Battaglia for numerous fruitful discussions and for sharing his enthusiasm. Warm thanks are due to Dr. Roberto Cirio and Dr. Peter Kluit for their co-authorship of physics analyses included in this thesis. I have also learned a lot during the work with the Vertex Detector and I am grateful to everybody, who participated in the building and the running of it. I owe a lot to Prof. Mårten Brenner for persuading me to study particle physics.

Many people in DELPHI and at SEFT have contributed, directly or indirectly, to the work presented in this thesis. Among others, I would like to acknowledge especially Prof. Ugo Amaldi, Prof. Jean-Eudes Augustin, Dr. Richard Brenner, Dr. Paula Collins, Dr. Jamaal Derkaoui, Dr. Hans Dijkstra, Dr. Magnus Karlsson, Doc. Reino Keränen, Dr. Dietrich Liko, Dr. Chiara Mariotti, Dr. Rego Ostonen, Kai Puolamäki, Doc. Heimo Saarikko, Dr. Raimo Vuopionperä and Dr. Agnieszka Zalewska. It has been a very pleasant and challenging environment to work in. The many valuable suggestions to the thesis from Prof. Masud Chaichian, Doc. Paula Eerola, Doc. Katri Huitu, Jari Pennanen and Craig Stocks are greatly appreciated. Finally, I want to thank my family and my girlfriend, Barbro, for their patience and understanding.

Contents

Introduction	3
List of Publications	4
Summary of the Original Publications	5
1 The Standard Model	7
1.1 The Tau Lepton and its Decays	12
2 New Physics in the Lepton Sector	16
2.1 Violation of Charged Lepton Universality	16
2.1.1 Charged Currents	17
2.1.2 Neutral Currents	19
2.2 Additional Leptons	20
2.3 Forbidden Decays	22
3 Experimental Tools and Techniques	25
3.1 The LEP Collider	25
3.2 The DELPHI Detector	25
3.2.1 Tracking	26
3.2.2 Luminosity Measurement and Calorimetry	28
3.2.3 Trigger and Data Acquisition System	29
3.2.4 The Ring Imaging Cherenkov Detectors	30
3.3 Charged Kaon Identification	34
3.3.1 Determination of the Cherenkov Angle and its Error	35
3.3.2 Kaons in τ Decays	37
4 Silicon Vertex Detectors	40
4.1 Design Considerations	40
4.2 The DELPHI Vertex Detector	42
4.2.1 Sensors	43
5 Software Development for the Vertex Detector	47
5.1 Cluster Reconstruction Issues	47
5.2 Improving Simulation Description	53
5.2.1 Efficiency Tables	54
5.2.2 Shaken Database	55
6 Conclusions	58

Introduction

Results from modern particle physics experiments confirm with a very high precision, the validity of the Standard Model, the theory of particle interactions, at currently achievable energy scales. Furthermore, the Standard Model has predicted both the existence of the massive weak W^\pm and Z^0 bosons, discovered by the UA1 and UA2 collaborations at CERN in 1983, and the top quark, discovered by the CDF and DO collaborations at Fermilab in 1995. However, most particle physicists believe that the Standard Model is only a low energy approximation of a more fundamental theory. This belief is based on well-motivated theoretical arguments, e.g. the large number of free parameters and no natural explanation for the mass hierarchy of quarks and leptons. Hence, it is natural to look for “new physics”, in order to obtain clues as to what the next development should be. New physics can be found either by performing a direct search for the anticipated types of signals, as is done in publications I and II, or by observing if the measurement of a standard phenomenon, such as in publications III and IV, shows a significant deviation from the Standard Model prediction.

In order to facilitate modern collider experiments, a large effort of research and development of new detector technologies is carried out. The techniques used in particle physics detectors can have also applications in areas of everyday life such as medicine. One of the most significant developments during the last decade are silicon detectors enabling high precision tracking. Publication V describes such a detector assembly.

The thesis is organized as follows. First, brief summaries of the appended publications are given. In chapter one the Standard Model is presented as well as the τ lepton and its decays. The following chapter gives a taste of possible new physics phenomena present in the lepton sector of the Standard Model. Next, the DELPHI detector is described with a special emphasis on the Ring Imaging Cherenkov (RICH) detectors as well as the experimental technique of charged kaon identification with the RICH, as used in publications III and IV. Chapters four and five deal with the aim and design of vertex detectors and with a few topics concerning the software development for the DELPHI Vertex Detector [1-3], focusing on issues not described in publication V. At the end of the thesis, the five research publications listed below are appended.

List of Publications

- I: P. Abreu et al. with K. Oesterberg,
Searches for heavy neutrinos from Z decays,
Physics Letters **B274** (1992) 230–238.
- II: P. Abreu et al. with K. Osterberg,
A search for lepton flavour violation in Z^0 decays,
Physics Letters **B298** (1993) 247–256.
- III: P. Abreu et al. with K. Osterberg,
Charged kaon production in tau decays at LEP,
Physics Letters **B334** (1994) 435–449.
- IV: K. Österberg for DELPHI Collaboration,
A measurement of τ decays into two charged Kaons,
DELPHI 95-66 PHYS 501 (EPS-HEP 95 #526) (30 June 1995).
- V: V. Chabaud et al. with K. Osterberg,
The DELPHI silicon strip microvertex detector with double sided readout,
Nuclear Instruments & Methods **A368** (1996) 314–332.

Summary of the Original Publications

Publication I: Searches for heavy neutrinos from Z decays. The simplest way to enlarge the Standard Model is to add another fermion family to the existing three and in analogy with the known families, one would expect that the lightest particle in the new family were a neutrino, belonging to an electroweak doublet together with the corresponding charged lepton (a so-called sequential neutrino). In this publication, the author of this thesis has performed an analysis, using the 1990 data taken by DELPHI, searching for such a neutrino which is not stable, but mixes with the known lepton doublets as the quark doublets are known to mix. Any sequential heavy neutrino having a mass up to almost half the Z^0 mass has been excluded using a combined analysis of the Z^0 line shape measurements and the results obtained in the direct search.

Publication II: A search for lepton flavour violation in Z^0 decays. One of the features of the Standard Model is the flavour diagonality of Z^0 processes (the so-called neutral currents). However, the theory does not provide any fundamental reason for the diagonality. The diagonality is manifested by the fact that Z^0 only couples to a fermion and anti-fermion pair of same flavour. The violation of the diagonality is present among quarks via charged current loops in the so-called penguin diagrams, but has not been observed for leptons, where the lepton flavour of each family is conserved separately. Lepton family flavour violating decays are expected in many extensions of the Standard Model. In this publication, the author of this thesis has carried out together with a colleague a search for non-flavour diagonal Z^0 decays into $e^\pm\mu^\mp$, $e^\pm\tau^\mp$ and $\mu^\pm\tau^\mp$ and upper limits on the branching ratios of these decays are set using the data collected with the DELPHI detector during the 1990 and 1991 runs.

Publication III: Charged kaon production in tau decays at LEP. Kaon production in weak decays of the τ lepton are Cabibbo-suppressed which is not expected for new superweak interactions. Therefore, it is interesting to measure the inclusive and exclusive decay rates of the τ lepton to kaons since the suppression makes them more sensitive to new physics. In this publication, kaon production in τ decays into one charged particle has been studied using the data taken during 1992, the first year of full Barrel RICH operation. The charged kaons were identified over a large momentum range using the RICH detector. Several branching ratios were determined and compared to the Standard Model prediction. In particular, the $\text{Br}(\tau^\pm \rightarrow \text{K}^\pm \nu_\tau)$ has been found to be in agreement with lepton universality and with other measurements [6]. The author of this thesis has made together with two colleagues the inclusive analysis and using the same method an exclusive analysis [4], not included in the publication.

Publication IV: A measurement of τ decays into two charged Kaons. In this conference contribution, the author of this thesis has studied kaon production in τ decays into three charged particles using the data taken with DELPHI between 1992 and 1994. The $\text{Br}(\tau^\pm \rightarrow \text{K}^\pm \text{K}^\mp \pi^\pm \nu_\tau \geq 0 \text{ neutrals})$ has been determined and found to be in agreement with the Standard Model prediction and other measurements [7,8].

Publication V: The DELPHI silicon strip microvertex detector with double sided readout. This publication describes the 1994-95 DELPHI vertex detector (the double sided upgrade of the detector) and its performance. All three coordinates have been reconstructed using a novel technique with AC coupled double sided silicon microstrip sensors. This technique enables the material to be kept to a minimum in the sensitive region, and therefore a good impact parameter resolution is retained also at lower momenta. The vertex detector and its upgrades [1-3] has significantly enlarged the physics potential of DELPHI. The author of this thesis has contributed to the software development for the vertex detector and has written the reconstruction and pattern recognition program for both upgrades. The participation of the author in the double sided upgrade has been more pronounced than for the original detector or the LEP2 upgrade, so the publication describing this detector is included in the thesis.

1 The Standard Model

The Standard Model (SM) of particle interactions includes the Glashow-Salam-Weinberg model [9], describing the electroweak interactions of quarks and leptons, and quantum chromodynamics (QCD) [10], describing the strong interactions of quarks. Gravity is excluded in this context, both due to the weakness of gravitational interactions at the elementary particle scale and due to the absence of a consistent gauge field theory description of it. The theoretical basis of the SM are relativistic and renormalizable gauge field theories expressed in Lagrangian formalism (see for example Ref. [11]). The physical conservation laws can be deduced from symmetry principles, which arise from the invariance of the Lagrangian and the physical vacuum under space-time or internal transformations. The spontaneous symmetry breaking of a local gauge symmetry generates masses for the gauge boson of the weak interaction, through the so-called Higgs mechanism [12], and at the same time provides masses for quarks and leptons via the Yukawa couplings.

In QCD each quark, the constituents of matter, possesses one of the three so-called colour charges, which reflects an underlying $SU(3)_C$ gauge symmetry. The gauge bosons of the theory, the massless gluons, couple to the colour charge and carry a superposition of two colour charges themselves. As a consequence of the gluons being coloured, QCD is a non-Abelian theory with gauge boson self-interaction. Unlike the electromagnetic coupling constant which increases with energy, the strong coupling constant decreases with energy, because the anti-screening effect of the gluon self-interactions dominate over the screening effect of the vacuum polarization. This behaviour of α_s leads to asymptotic freedom of quarks at high energies and presumably to quark confinement at low energies. The $SU(3)_C$ symmetry is believed to be exact.

The electroweak model is based on the $SU(2)_L \otimes U(1)_Y$ gauge symmetry spontaneously broken to the residual $U(1)_{em}$ symmetry of electromagnetic interaction. To have spontaneous symmetry breaking scalar particles, Higgs bosons, have to be included in the model. The particle spectrum of the SM consists of scalar Higgs particles, vector

bosons and spin-1/2 fermions. All known fermions, i.e. leptons (ν, l) and quarks (u, d), are grouped into three fermion families and so far there are no indications that more families exist, although it is not excluded. Under the $SU(2)_L \otimes U(1)_Y \otimes SU(3)_C$ gauge symmetry each fermion family ($k = 1, 2, 3$) has the following field contents (the colour indices of the quark fields are suppressed):

$$\begin{aligned}
L_{kL} &= \begin{pmatrix} \nu_{\ell_k} \\ \ell_k \end{pmatrix}_L \sim (2, -1, 1), & \ell_{kR} &\sim (1, -2, 1), \\
Q_{kL} &= \begin{pmatrix} u_k \\ d_k \end{pmatrix}_L \sim (2, \frac{1}{3}, 3), & u_{kR} &\sim (1, \frac{4}{3}, 3), & d_{kR} &\sim (1, -\frac{2}{3}, 3).
\end{aligned} \tag{1}$$

The numbers inside the parentheses indicate the representations of the fields under the different gauge symmetries, or in the case of the $U(1)_Y$ symmetry, the value of Y , the so-called hypercharge. The leptonic fields are, for example, represented as singlets under the $SU(3)_C$ symmetry i.e. are not affected by a $SU(3)_C$ transformation indicating that strong interaction is not felt by the leptons. The $SU(2)_L$ weak interactions are of the $V - A$ form [13], which allows only left-handed $SU(2)$ -doublets, indicated by index L , and therefore the right-handed fermions are added as $SU(2)$ -singlets. The electroweak model neither prevents nor predicts the existence of right-handed neutrinos but in the minimal SM they are usually left out since their existence has no experimental support. The electric charge, Q , the generator of the residual $U(1)_{em}$ symmetry, can be defined as

$$Q = T_3 + \frac{Y}{2}, \tag{2}$$

where T_3 is one of the three generators of the $SU(2)_L$ symmetry. $T = 1/2$ for a doublet representation and $T = 0$ for a singlet representation.

The scalar sector of the SM consists of a Higgs doublet

$$\phi \equiv \begin{pmatrix} \phi^+ \\ \phi^0 \end{pmatrix} \sim (2, 1, 1), \tag{3}$$

where the neutral component acquires vacuum expectation value, thereby breaking the electroweak symmetry. This is the minimal case, but in general the Higgs sector may

be more complicated. In the minimal supersymmetric version of the SM (MSSM) [14], for example there should at least exist two scalar doublets.

The Lagrangian of the SM is of the form

$$\mathcal{L} = \mathcal{L}_{\text{kin}}^{\text{matter}} + \mathcal{L}_{\text{kin}}^{\text{gauge}} + \mathcal{L}_{\text{Yukawa}} - V(\phi). \quad (4)$$

The kinetic term for the matter fields is given by

$$\begin{aligned} \mathcal{L}_{\text{kin}}^{\text{matter}} = & \left| \left(\partial_\mu i g \mathbf{T} \cdot \mathbf{W}_\mu - i \frac{g'}{2} B_\mu \right) \phi \right|^2 \\ & + i \bar{Q}_{kL} \gamma^\mu \left(\partial_\mu - i g \mathbf{T} \cdot \mathbf{W}_\mu - i \frac{g'}{6} B_\mu \right) Q_{kL} \\ & + i \bar{u}_{kR} \gamma^\mu \left(\partial_\mu - i \frac{2g'}{3} B_\mu \right) u_{kR} + i \bar{d}_{kR} \gamma^\mu \left(\partial_\mu + i \frac{g'}{3} B_\mu \right) d_{kR} \\ & + i \bar{L}_{kL} \gamma^\mu \left(\partial_\mu i g \mathbf{T} \cdot \mathbf{W}_\mu + i \frac{g'}{2} B_\mu \right) L_{kL} + i \bar{\ell}_{kR} \gamma^\mu \left(\partial_\mu + i g' B_\mu \right) \ell_{kR}, \end{aligned} \quad (5)$$

where g and g' are the coupling constants of the $SU(2)_L$ and $U(1)_Y$ symmetries and are related to the residual $U(1)_{\text{em}}$ symmetry coupling constant, e , and the so-called weak mixing angle, θ_W , by

$$g \sin \theta_W = g' \cos \theta_W = e. \quad (6)$$

The kinetic term for the gauge fields is given by

$$\mathcal{L}_{\text{kin}}^{\text{gauge}} = -\frac{1}{4} \mathbf{W}_{\mu\nu} \cdot \mathbf{W}^{\mu\nu} - \frac{1}{4} B_{\mu\nu} B^{\mu\nu}, \quad (7)$$

where

$$\mathbf{W}_{\mu\nu} \equiv \partial_\mu \mathbf{W}_\nu - \partial_\nu \mathbf{W}_\mu + g \mathbf{W}_\mu \times \mathbf{W}_\nu \quad \text{and} \quad B_{\mu\nu} \equiv \partial_\mu B_\nu - \partial_\nu B_\mu. \quad (8)$$

\mathbf{W}_μ stands for $(W_{1\mu}, W_{2\mu}, W_{3\mu})$, the three gauge bosons of the $SU(2)_L$ symmetry, and B_μ for the gauge boson of the $U(1)_Y$ symmetry.

The Yukawa terms describing the interactions of quarks and leptons with the Higgs scalars are given by the Lagrangian

$$\mathcal{L}_{\text{Yukawa}} = -(h_d)_{kj} \bar{Q}_{kL} \phi d_{jR} - (h_u)_{kj} \bar{Q}_{kL} \tilde{\phi} u_{jR} - (h_l)_{kj} \bar{L}_{kL} \phi \ell_{jR} + h.c., \quad (9)$$

where h_d , h_u and h_l are dimensionless Yukawa couplings and the charge conjugate of the scalar field is defined as $\tilde{\phi} = i\tau_2 \phi^* \sim (2, -1, 1)$. As can be seen from (9) there is no

term giving mass to the neutrinos and therefore in the minimal SM, the neutrinos are massless. However, if right-handed neutrinos exist, terms such as $-(h_\nu)_{kj} \bar{L}_{kL} \tilde{\phi} \nu_{jR}$ can be added to (9) and thus neutrinos can also acquire mass in the SM.

The Higgs potential is chosen to be

$$V(\phi) = -\mu^2(\phi^\dagger\phi) + \frac{\lambda}{4}(\phi^\dagger\phi)^2, \quad \mu^2 > 0, \quad \lambda > 0. \quad (10)$$

The minimum of this potential corresponds to the vacuum expectation value

$$\langle\phi\rangle = \frac{1}{\sqrt{2}} \begin{pmatrix} 0 \\ v \end{pmatrix} \quad (11)$$

of the scalar doublet, where $v = 2\mu/\sqrt{\lambda}$. The vacuum breaks the electroweak symmetry $SU(2)_L \otimes U(1)_Y$, except the $U(1)_{\text{em}}$ subsymmetry associated with the electromagnetism. The gauge bosons, W^\pm and Z^0 , corresponding to the broken generators acquire mass [9], while the photon, the gauge boson corresponding to the unbroken generator of $U(1)_{\text{em}}$, remains massless. In other words, the SM symmetry $SU(2)_L \otimes U(1)_Y \otimes SU(3)_C$ is spontaneously broken down to the $U(1)_{\text{em}} \otimes SU(3)_C$ residual gauge symmetry. The masses of the weak bosons W^\pm and Z^0 are

$$m_W = \frac{gv}{2}, \quad m_Z = \frac{v\sqrt{g^2 + g'^2}}{2} = \frac{m_W}{\cos\theta_W}. \quad (12)$$

Three components of the scalar field are re-gauged to give masses to the weak gauge bosons, but the remaining one acquires mass, $m_H = \sqrt{2\mu^2}$, to become the Higgs boson. The Higgs boson has not been observed experimentally and the current lower limit at 95 % confidence level on its mass from LEP searches, is 77.5 GeV/ c^2 [16].

Thus, in terms of the physical gauge fields the interaction Lagrangian is given by

$$\mathcal{L} = -e J_{\text{em}}^\mu A_\mu - \sqrt{g^2 + g'^2} J_{\text{NC}}^\mu Z_\mu - \frac{g}{2\sqrt{2}} (J_{\text{CC}}^\mu W_\mu^+ + J_{\text{CC}}^{\mu\dagger} W_\mu^-) \quad (13)$$

where

$$J_{\text{NC}}^\mu = J_3^\mu - \sin^2\theta_W J_{\text{em}}^\mu, \quad (14)$$

$$J_{\text{CC}}^\mu = 2(\bar{\nu}_L \gamma^\mu \ell_L + \bar{u}_L \gamma^\mu d_L), \quad (15)$$

$$J_{\text{em}}^\mu = -\bar{\ell} \gamma^\mu \ell + \frac{2}{3} \bar{u} \gamma^\mu u - \frac{1}{3} \bar{d} \gamma^\mu d, \quad (16)$$

$$J_3^\mu = -\frac{1}{2} \bar{\ell}_L \gamma^\mu \ell_L + \frac{1}{2} \bar{\nu}_L \gamma^\mu \nu_L - \frac{1}{2} \bar{d}_L \gamma^\mu d_L + \frac{1}{2} \bar{u}_L \gamma^\mu u_L. \quad (17)$$

$\sin^2 \theta_W$ is experimentally determined by a combined LEP measurement to be $0.2315 \pm 0.0002 \pm 0.0003$ [17].

The quark fields appearing in the above interaction Lagrangian, the so-called weak eigenstates, do not correspond to the physical quark mass eigenstates. By convention, the transformations for the down type d' , s' , b' quark mass eigenstates are described by a unitary 3×3 matrix, $V_{qq'}^{\text{CKM}}$, called the Cabibbo-Kobayashi-Maskawa (CKM) mixing matrix [18]:

$$\begin{pmatrix} d' \\ s' \\ b' \end{pmatrix} = \begin{pmatrix} V_{ud} & V_{us} & V_{ub} \\ V_{cd} & V_{cs} & V_{cb} \\ V_{td} & V_{ts} & V_{tb} \end{pmatrix} \begin{pmatrix} d \\ s \\ b \end{pmatrix}. \quad (18)$$

A similar matrix, $V_{\nu l}^{\text{CKM}}$, can be defined for the leptons. The move from the interaction basis of the fermion fields into the mass basis will only change the form of the charged current part of the gauge Lagrangian (13). It will now be of the form:

$$J_{CC}^\mu = 2 \left[\bar{\nu}_{jL} (V_{\nu l}^{\text{CKM}})_{jk} \gamma^\mu \ell'_{kL} + \bar{u}_{jL} (V_{qq'}^{\text{CKM}})_{jk} \gamma^\mu d'_{kL} \right]. \quad (19)$$

The diagonal elements of the $V_{qq'}^{\text{CKM}}$ matrix are close to one, whereas the off-diagonal elements are smaller than one, disavouring such transitions, referred to as Cabibbo-suppressed, by the square of the element. The $V_{qq'}^{\text{CKM}}$ matrix, except for the elements involving the top quark, is experimentally quite well known [18]. In contrast, the elements of the lepton mixing matrix $V_{\nu l}^{\text{CKM}}$ are almost unknown [19]. The mixing formalism is valid for any number n_f of fermion families and the CKM matrices can be parameterized in terms of $\frac{1}{2}n_f(n_f - 1)$ rotational angles and $\frac{1}{2}(n_f - 1)(n_f - 2)$ phases [11,20]. In the case of three families, this means three rotation angles and one phase.

The non-diagonal nature of the charged currents permits flavour changing reactions, such as $K^+ \rightarrow \mu^+ \nu_\mu$, where one has the transition $\bar{s} \rightarrow \bar{d}$ [21], while CP violating reactions, such as $K_L^0 \rightarrow \pi^+ \pi^-$ [22], arise because of the complex phase in the mixing matrix. Flavour changing neutral current and CP violating reactions have been observed in the quark sector [23], but never in the lepton sector, where the very small neutrino mass forces them to be negligible. If neutrinos do not have mass, there is neither flavour changing neutral currents nor CP violating reactions in the lepton sector because the mass eigenstates of the leptons are, in this case, the same as the current eigenstates.

The SM is experimentally very precisely verified [17] and has successfully predicted the existence of the massive gauge bosons, W^\pm and Z^0 . However, the existence and structure of the Higgs sector is a completely open question. Furthermore, it seems like a mere coincidence that the Higgs mass would be of the same order as the electroweak scale, since the radiative corrections to masses of scalar particles are proportional to the scale of physics beyond the SM, e.g. the grand unification scale ($\sim 10^{15}$ GeV) or the Planck scale ($\sim 10^{19}$ GeV). This fine-tuning requirement of the corrections is the so-called naturalness problem. In addition, the SM does not explain the family structure and the hierarchy of quark and lepton masses. There are also an unnaturally large amount of free parameters in the SM, altogether 18 in the minimal SM. They are

- the six Yukawa couplings fixing the masses of the different quarks
- the three Yukawa couplings fixing the masses of the different charged leptons
- the three gauge symmetry couplings constants fixing the strength of the interactions
- the three rotation angles and the phase of the $V_{qq'}^{\text{CKM}}$ matrix fixing the relation between weak and mass eigenstates of the quarks
- the μ^2 and λ parameters of the Higgs potential, fixing the Higgs and gauge boson mass scales

All these indicate that the SM is only a partial answer to an ultimate theory of particle interactions.

1.1 The Tau Lepton and its Decays

The τ lepton has been studied extensively since its discovery in 1975 [24] and a comprehensive list of its properties is given in Ref. [25]. In the SM, the τ is included in a left-handed weak doublet with its associated neutrino, and in a right-handed singlet as shown in (1). The τ lepton and its neutrino have their own conserved lepton number. It is the heaviest known lepton and the only one massive enough to decay to hadrons. Therefore, the τ is a perfect tool to study weak interactions under simple conditions,

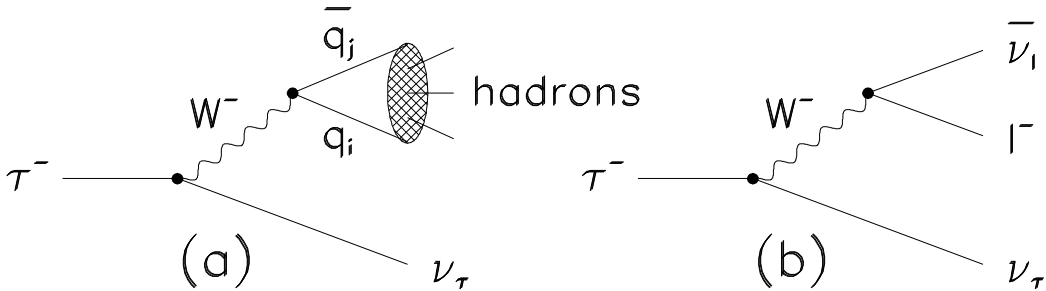


Figure 1: Feynman diagrams of τ decay (a) to hadrons and (b) to leptons.

to test the universality of the weak interactions and to investigate the formation of resonant hadronic states. It may also be a sensitive probe of physics beyond the SM. The mass of the τ lepton has been determined from a detailed measurement of the τ production cross section, $\sigma(e^+ e^- \rightarrow \tau^+ \tau^-)$, near the production threshold and is $1777.00_{-0.27}^{+0.30}$ MeV/ c^2 [25]. The τ lifetime determination is dominated by decay path measurements made at LEP, benefiting from the good spatial resolution obtained using silicon vertex detectors. The current world average value is 290.34 ± 1.15 fs [5].

The decays of the τ lepton are described within the SM by the Feynman diagrams shown in Figure 1. The leptonic decay modes of the τ lepton are well understood and have contributed to the understanding of electroweak decays. The width of the leptonic decay, taking into account first order electroweak corrections, and assuming the neutrino to be massless [26], is given as:

$$\Gamma(\tau \rightarrow l \bar{\nu}_l \nu_\tau) = \frac{G_F^2 m_\tau^5}{192 \pi^3} f\left(\frac{m_l^2}{m_\tau^2}\right) \left[1 + \frac{3 m_\tau^2}{5 m_W^2}\right] \left[1 + \frac{\alpha(m_\tau)}{2 \pi} \left(\frac{25}{4} - \pi^2\right)\right], \quad (20)$$

where $\alpha(m_\tau) = 1/133.3$ is the running coupling constant of electromagnetism at the τ mass scale, $G_F = g^2 / (4 \sqrt{2} m_W^2)$ is the Fermi coupling constant for weak interactions. The function $f(y)$ accounts for non-zero masses of the final state leptons:

$$f(y) = 1 - 8y + 8y^3 - y^4 - 12y^2 \ln y. \quad (21)$$

For τ decay into electron $f(y)$ is essentially one, whereas for decay into muon $f(y) = 0.9726$. The branching ratio for decay a is related to the decay width by $\text{Br}_a = \Gamma_a \tau_\tau / \hbar$, where τ_τ is the lifetime of the τ lepton.

Contrary to leptonic decay modes, the hadronic decay modes are less well known but can be predicted with a few theoretical assumptions. Table 1 lists a few of the measured branching ratios [5-8] with the theoretical predictions [26-31]. The theoretical predictions have been updated using the τ lifetime of Ref. [5] and in several cases the error on the τ lifetime constitutes the biggest contribution to the uncertainty. In the predictions of the decay modes with three particles in the final state, a large uncertainty comes from the widths and the masses of the resonances and also with which relative fraction a resonance contributes to a certain final state.

Table 1: A few important τ decay rates with measurements and predictions

Decay mode	Branching ratio (%)	Theoretical prediction (%)
$\tau^\pm \rightarrow e^\pm \bar{\nu}_e \nu_\tau$	17.817 ± 0.074	17.786 ± 0.070
$\tau^\pm \rightarrow \mu^\pm \bar{\nu}_\mu \nu_\tau$	17.338 ± 0.085	17.298 ± 0.068
$\tau^\pm \rightarrow \pi^\pm \nu_\tau$	11.09 ± 0.15	10.90 ± 0.05
$\tau^\pm \rightarrow K^\pm \nu_\tau$	0.68 ± 0.04	0.715 ± 0.004
$\tau^\pm \rightarrow \rho^\pm \nu_\tau$	24.91 ± 0.21	25.0 ± 1.1
$\tau^\pm \rightarrow K^{*\pm}(892) \nu_\tau$	1.36 ± 0.08	1.20 ± 0.05
$\tau^\pm \rightarrow \pi^\pm \pi^\mp \pi^\pm \nu_\tau$	8.64 ± 0.24	9.2
$\tau^\pm \rightarrow K^\pm \pi^\mp \pi^\pm \nu_\tau$	0.29 ± 0.04	0.45
$\tau^\pm \rightarrow K^\pm K^\mp \pi^\pm \nu_\tau$	0.17 ± 0.02	0.20

The charged current has both vector and axial vector components in the framework of the SM and can thereby couple to hadronic states with spin-parity $J^P = 0^-, 0^+, 1^-, 1^+$. The general form of hadronic τ decays can be written as [27]:

$$\Gamma(\tau \rightarrow \text{hadrons} + \nu_\tau) = \frac{G_F^2}{32 \pi^2 m_\tau^3} \int_0^{m_\tau^2} dq^2 (m_\tau^2 - q^2)^2 \times \\ \left\{ |V_{ud}|^2 \left[(m_\tau^2 + 2q^2)(v_1(q^2) + a_1(q^2)) + m_\tau^2 a_0(q^2) \right] + \right. \\ \left. |V_{us}|^2 \left[(m_\tau^2 + 2q^2)(v_1^s(q^2) + a_1^s(q^2)) + m_\tau^2 (v_0^s(q^2) + a_0^s(q^2)) \right] \right\}, \quad (22)$$

where V_{ud} and V_{us} are the CKM matrix elements, $v^{(s)}$ and $a^{(s)}$ are the vector and axial vector spectral functions of q^2 , where q is the invariant mass of the hadronic system.

The subscripts of these functions denote the spin J of the hadronic system and the superscript s denotes a system with net strangeness. Since τ lepton decays have low q^2 ($q^2 < m_\tau^2$), the spectral functions are expected to be dominated by individual hadronic resonances. The possible hadronic states are given in Table 2 with the corresponding spectral functions.

Table 2: Allowed quantum numbers and resonances for hadronic τ decays

Spectral function	Spin-Parity	Hadronic resonances
v_1	1^-	$\rho^\pm (770), \rho^\pm (1700)$
a_1	1^+	$a_1^\pm (1260)$
a_0	0^-	π^\pm
v_1^s	1^-	$K^{*\pm} (892)$
a_1^s	1^+	$K_1^\pm (1270), K_1^\pm (1400)$
a_0^s	0^-	K^\pm
v_0^s	0^+	$K_0^\pm (1430)$

The spectral functions cannot be calculated directly since perturbative QCD is not valid at such low energies, but they can be obtained using the factorization property. The Conserved Vector Current (CVC) theorem states that $v_0(q^2) = 0$ and $v_1(q^2)$ can be related to the total hadronic cross section by $v_1(q^2) = q^2 \sigma_{I=1}(e^+e^- \rightarrow \text{hadrons})/4\pi\alpha^2$. The Weinberg sum rules [32] on the other hand, provide a relation between $v_1(q^2)$ and $a_1(q^2)$ and the Das, Mathur and Okubo (DMO) sum rules [33] relates $v_1^s(q^2)$ and $a_1^s(q^2)$ to $v_1(q^2)$. The two sum rules predicts that $f_\rho = f_{a_1}$, $f_\rho^2/m_\rho^2 = f_{K^*}^2/m_{K^*}^2$ and $f_{a_1}^2/m_{a_1}^2 = f_{K_1}^2/m_{K_1}^2$, where the f 's are the respective decay constants. For instance, if the spectral functions $v_1^s(q^2)$ and $v_0^s(q^2)$ are estimated to be $2\pi (f_{K^*}/m_{K^*})^2 \delta(q^2 - m_{K^*}^2)$ and $2\pi f_K^2 \delta(q^2 - m_K^2)$ respectively, then the corresponding decay widths, using the approximation $f_\rho^2 \approx m_\rho^4/4\pi$ [27], are:

$$\begin{aligned}
\Gamma(\tau \rightarrow K^*(892) \nu_\tau) &= \frac{G_F^2}{64 \pi^2} |V_{us}|^2 m_\tau^3 m_\rho^2 \left[1 - \frac{m_{K^*}^2}{m_\tau^2}\right]^2 \left[1 + \frac{2 m_{K^*}^2}{m_\tau^2}\right] \\
\Gamma(\tau \rightarrow K \nu_\tau) &= \frac{G_F^2}{16 \pi} |V_{us}|^2 m_\tau^3 f_K^2 \left[1 - \frac{m_K^2}{m_\tau^2}\right]^2.
\end{aligned} \tag{23}$$

2 New Physics in the Lepton Sector

As pointed out in the first chapter, though the Standard Model (SM) describes the experimental data very well, it has many shortcomings. Some of these shortcomings seem to indicate a further unification of electro-weak and strong interactions in the so-called grand unified theories (GUT) [34], and some seem to suggest supersymmetry [14], compositeness [35] or the so-called technicolour models [36]. The motivation for most models are that they can give a natural explanation to at least some of the shortcomings of the SM. However, any extended model should contain the SM particles or they should at least naturally come out in the model, and the gauge symmetry of any extended gauge model should eventually break down to the SM gauge group. Furthermore, the extended models should not alter the successful predictions of the SM in order that they would be in agreement with the experimental measurements. Most of the models mentioned above predict new physics in the lepton sector.

Also the SM itself allows new phenomena in the lepton sector such as masses for neutrinos or additional families. The topics discussed here are going to be the violation of charged lepton universality, additional leptons and rare or forbidden decays. This is by no means a comprehensive list of possible new phenomena, but merely a list of new phenomena present in many of the extended models and therefore interesting phenomena to search for.

2.1 Violation of Charged Lepton Universality

Charged lepton universality asserts that modulo mass effects, the electron, muon and tau leptons all exhibit identical properties. In the SM, universality is naturally realized by the gauge interactions since the three families of leptons all have the same $SU(2)_L \otimes U(1)_Y$ transformation properties and quantum numbers. As a consequence, their bare gauge couplings and electric charges must be the same. The radiative corrections [26] in the SM will only differ for the three species because the masses are different, but these

can easily be accounted for when making comparisons. Non-universality could then be due to new interactions or loops with new particles that violate the universality. The non-universality would manifest itself differently in comparisons, depending on the way the universality is violated and with which strength.

2.1.1 Charged Currents

The most common test of the universality of the $SU(2)_L$ gauge coupling is the comparison of charged current reactions involving only leptons. The test of the $\mu - \tau$ universality is made by comparing the leptonic tau decays $\tau \rightarrow l \bar{\nu}_l \nu_\tau(\gamma)$ ($l = e, \mu$) with $\mu \rightarrow e \bar{\nu}_e \nu_\mu(\gamma)$, where (γ) always denotes inclusion of decays with additional photons. Using (20) and a similar equation for the muon decay obtained by doing the exchanges $m_\tau \rightarrow m_\mu$ and $m_l \rightarrow m_e$ in (20), gives

$$\left(\frac{g_\tau}{g_\mu}\right)^2 = \frac{\tau_\mu}{\tau_\tau} \left(\frac{m_\mu}{m_\tau}\right)^5 \text{Br}(\tau \rightarrow l \bar{\nu}_l \nu_\tau(\gamma)) \Delta_\gamma \Delta_W, \quad (24)$$

where $\Delta_\gamma = 1 + 8.6 \times 10^{-5}$ and $\Delta_W = 1 - 3.0 \times 10^{-4}$ are the relative differences between the electroweak radiative corrections [26]. Using the compilation [5] of the measurements from the LEP experiments and the CLEO detector [37] and correcting for masses, a ratio $g_\tau/g_\mu = 1.0010 \pm 0.0025$ is obtained. The $e - \mu$ universality can be tested by computing the ratio of $\text{Br}(\tau \rightarrow \mu \bar{\nu}_\mu \nu_\tau(\gamma))$ and $\text{Br}(\tau \rightarrow e \bar{\nu}_e \nu_\tau(\gamma))$ and correcting for the phase space factor due to the m_μ . This gives $g_\mu/g_e = 0.9997 \pm 0.0032$.

Hadronic τ decays provide an independent way to test $\mu - \tau$ universality. In practice, since the knowledge of the QCD part contained in the decay constant is required, only decays into stable pseudoscalar mesons can be used for this purpose by comparing the rate for $\tau \rightarrow P \nu_\tau(\gamma)$ and $P \rightarrow \mu \bar{\nu}_\mu(\gamma)$, where P is a pion or a kaon. The expression in the pion case is

$$\left(\frac{g_\tau}{g_\mu}\right)^2 = \frac{\tau_\pi}{\tau_\tau} \frac{2 m_\pi m_\mu^2}{m_\tau^3} \left(\frac{1 - \frac{m_\mu^2}{m_\pi^2}}{1 - \frac{m_\mu^2}{m_\tau^2}}\right)^2 \frac{\text{Br}(\tau \rightarrow \pi \nu_\tau(\gamma))}{\Delta_\pi \text{Br}(\pi \rightarrow \mu \bar{\nu}_\mu(\gamma))}, \quad (25)$$

where Δ_π is the relative radiative correction for the two processes, which has been evaluated to be $1 + (1.6 \pm 1.4) \times 10^{-3}$ including radiation from the composite π system [28]. A similar expression is obtained for the kaon by replacing π by K and Δ_π by $\Delta_K =$

$1 + (9.0 \pm 2.2) \times 10^{-3}$ in (25). The values listed in Table 1 give $g_\tau/g_\mu = 1.0087 \pm 0.0072$ and $g_\tau/g_\mu = 0.975 \pm 0.029$ for the pion and kaon cases, respectively. The measurement in publication III of the $\text{Br}(\tau \rightarrow \text{K}\nu_\tau(\gamma))$ gives $g_\tau/g_\mu = 1.09 \pm 0.11$.

Due to the precise theoretical predictions for the τ branching ratios mentioned above, their measurements can be sensitive to interactions beyond the SM. Many models attempt to unify the known interactions and several of them predict additional superweak interactions (SW). The couplings of these new interactions can be different for fermions of different families, e.g. through mixing or couplings which are mass dependent, and as a result the charged lepton universality may be violated. If the new interaction is mediated by a spin one boson with a similar propagator as the weak W boson, the charged current part of the gauge Lagrangian (13) could be of the form:

$$J_{\text{CC}(\text{SM}+\text{SW})}^\mu = 2[f_1 \bar{\nu}_L \gamma^\mu \ell_L + f_d \bar{u}_L \gamma^\mu d_L + f_s \bar{u}_L \gamma^\mu s_L + f'_1 \bar{\nu}_L \gamma'^\mu \ell_L + f'_d \bar{u}_L \gamma'^\mu d_L + f'_s \bar{u}_L \gamma'^\mu s_L], \quad (26)$$

where the terms in the first line represents the normal weak interaction and the terms in the second line the additional superweak interaction. The f 's are the relative coupling strength of the charged current vertex with respect to the leptonic one, i.e. $f_1 = 1$, $f_s = |V_{us}|$, $f_d = |V_{ud}|$. The f' 's describing the relative strength of the new interaction are unknown, but the assumption $f' \ll 1$ should be valid since the decays are dominated by the normal weak interaction. Each SM decay width involving a charged lepton and a pseudoscalar meson will be modified so that

$$\Gamma_{\text{SM}+\text{SW}} = \Gamma_{\text{SM}} \left(1 + \frac{2 f'_q f'_1}{f_q f_1} + \frac{f_q'^2 f_1'^2}{f_q^2 f_1^2} \right). \quad (27)$$

The ratio of the decay widths with the assumption $f' \ll 1$ will have the form:

$$\left[\frac{\Gamma(\tau \rightarrow \text{P} \nu_\tau(\gamma))}{\Gamma(\text{P} \rightarrow \mu \bar{\nu}_\mu(\gamma))} \right]_{\text{SM}+\text{SW}} = \left[\frac{\Gamma(\tau \rightarrow \text{P} \nu_\tau(\gamma))}{\Gamma(\text{P} \rightarrow \mu \bar{\nu}_\mu(\gamma))} \right]_{\text{SM}} \left(1 + \frac{2 f'_q}{f_q} (f'_\tau - f'_\mu) + \mathcal{O}(f'^2) \right). \quad (28)$$

A similar expression can be obtained for the ratio between the decay widths of $\tau \rightarrow e \bar{\nu}_e \nu_\tau(\gamma)$ and $\mu \rightarrow e \bar{\nu}_e \nu_\mu(\gamma)$. Due to the presence of f_q , corresponding to the Cabibbo-suppression, in the denominator in (28), it is obvious that the $\tau \rightarrow \text{K} \nu_\tau(\gamma)$ is particularly sensitive to lepton universality violating interactions of the type given

above. The natural assumption that $f'_\tau \gg f'_\mu$ makes it interesting to extract an upper limit on the first order term in (28) using the experimental measurements. The 95 % CL upper limits on the first order term, obtained using for the different decay modes the experimental values listed in Table 1, are given in Table 3. The measurement in publication III of the $\text{Br}(\tau \rightarrow \text{K} \nu_\tau(\gamma))$ gives a 95 % CL limit of $f'_s (f'_\tau - f'_\mu) < 0.07 G_F$, where G_F is the Fermi coupling constant.

Table 3: 95 % CL limits on new superweak interactions from τ decays

Decay width ratio	Limit (in units of G_F)
$\frac{\Gamma(\tau \rightarrow e \bar{\nu}_e \nu_\tau(\gamma))}{\Gamma(\mu \rightarrow e \bar{\nu}_e \nu_\tau(\gamma))}$	$f'_e (f'_\tau - f'_\mu) < 0.006$
$\frac{\Gamma(\tau \rightarrow \text{K} \nu_\tau(\gamma))}{\Gamma(\text{K} \rightarrow \mu \bar{\nu}_\mu(\gamma))}$	$f'_s (f'_\tau - f'_\mu) < 0.009$
$\frac{\Gamma(\tau \rightarrow \pi \nu_\tau(\gamma))}{\Gamma(\pi \rightarrow \mu \bar{\nu}_\mu(\gamma))}$	$f'_d (f'_\tau - f'_\mu) < 0.02$

Precision measurements of the leptonic branching ratios of the τ lepton might reveal information about e.g. supersymmetric models or any model with two Higgs doublets [38]. The tree-level charged Higgs (H^\pm) exchange reduces the leptonic branching ratio predictions of (20) by about a factor $\left[1 - \left(m_\tau m_1 / m_{H^\pm}^2\right) \tan^2 \beta\right]$, where $\tan \beta$ is the ratio of the two vacuum expectation values. If $\tan \beta$ is large ($\tan \beta > 20$) and $m_{H^\pm} \sim m_{W^\pm}$, then the $\text{Br}(\tau \rightarrow \mu \bar{\nu}_\mu \nu_\tau(\gamma))$ is reduced by about 0.1 % from the SM model value. Slightly smaller changes could be caused by large mass differences between the different species of sleptons, the supersymmetric partners of leptons.

2.1.2 Neutral Currents

Very precise tests of charged lepton universality in neutral current couplings are provided by the partial decay widths of the Z^0 boson, $\Gamma(Z^0 \rightarrow l^+ l^-) \equiv \Gamma_l$, and the angular decay asymmetries. The partial decay widths (including first order radiative corrections) are predicted to be:

$$\Gamma(Z^0 \rightarrow l^+ l^-(\gamma)) = \frac{G_F m_{Z^0}^3 \beta}{6 \sqrt{2} \pi} \left[\bar{g}_{V1}^2 \left(\frac{3 - \beta^2}{2} \right) + \bar{g}_{A1}^2 \beta^2 \right] \left[1 - \frac{3 \alpha(m_{Z^0})}{4 \pi} \right], \quad (29)$$

where $\bar{g}_{V1} = \frac{1}{2}\sqrt{\rho} (1 - 4\kappa \sin^2 \theta_W)$ and $\bar{g}_{A1} = \frac{1}{2}\sqrt{\rho}$ are the effective vector and axial vector couplings, respectively. $\rho = 1 + \rho_t$ and $\kappa = 1 + \rho_t/\tan^2 \theta_W$ are the relative electroweak-radiative corrections with the top quark and Higgs boson mass dependence imbedded in the ρ_t factor. The Z^0 decay asymmetries measure the combination

$$A_1 = \frac{2\bar{g}_{V1}\bar{g}_{A1}}{\bar{g}_{V1}^2 + \bar{g}_{A1}^2}. \quad (30)$$

The forward-backward asymmetries determine $A_1^{FB} = \frac{3}{4} A_e A_1$, whereas the polarization studies in τ lepton decays separate A_τ and A_e . The latest compilation of the LEP measurements [39] gives $\bar{g}_{V1} = -0.03681 \pm 0.00085$ and $\bar{g}_{A1} = -0.50112 \pm 0.00032$ with the lepton universality assumption. The tests of the lepton universality give the following ratios between the vector and axial vector couplings for different charged leptons: $\bar{g}_{V\mu}/\bar{g}_{Ve} = 1.02 \pm 0.12$, $\bar{g}_{V\tau}/\bar{g}_{Ve} = 0.998 \pm 0.060$, $\bar{g}_{A\mu}/\bar{g}_{Ae} = 0.9993 \pm 0.0017$ and $\bar{g}_{A\tau}/\bar{g}_{Ae} = 0.9996 \pm 0.0018$.

From the partial decay widths bounds can be put on the anomalous magnetic and electric dipole moments of leptons [40]. Such dipole moments could be introduced by, for example, composite models modifying the SM Lagrangian (4) by ($k = e, \mu, \tau$):

$$\delta\mathcal{L} = \frac{\alpha_{kB}}{\Lambda^2} \bar{L}_{kL} \sigma^{\mu\nu} \ell_{kR} \phi B_{\mu\nu} + \frac{\alpha_{kW}}{\Lambda^2} \bar{L}_{kL} \sigma^{\mu\nu} \tau \ell_{kR} \phi \mathbf{W}_{\mu\nu}, \quad (31)$$

where ϕ is the Higgs doublet, α_{kB} and α_{kW} are unknown coupling constants and Λ the mass scale of new physics. The anomalous magnetic dipole moment a_1 is altered after electroweak symmetry breaking due to (31) by $\delta a_1 \propto \alpha_{1B(1W)}/\Lambda^2$. The change on the partial width, $\delta\Gamma_1$, and δa_1 are related as:

$$\frac{e}{2m_1} |\delta a_1| = \cot \theta_W \sqrt{\frac{24\pi |\delta\Gamma_1|}{m_{Z^0}^3 \beta}}. \quad (32)$$

A similar argument holds for the electric dipole moment, d_1 . For the τ lepton in the SM, a_τ is expected to be 1.177×10^{-3} [41] and d_τ extremely small. The LEP Γ_τ measurement gives $|\delta a_\tau| \leq 4.8 \times 10^{-3}$ and $|d_\tau| \leq 2.7 \times 10^{-17} e \text{ cm}$ [40]. A slightly better bound on d_τ gives searches for CP violation in the $Z^0 \rightarrow \tau^+ \tau^-$ decay [42].

2.2 Additional Leptons

Additional leptons, with respect to the three known doublets, are predicted by various theories [43] but have not been observed so far. The most common way to include new

leptons is either through a weak isospin doublet or a singlet. An additional doublet would naturally suggest the existence of a complete fourth family of fermions, though the SM allows different number of families for leptons and quarks. However, from a theoretical point of view a fourth family seems unattractive since three families is the minimal structure needed to have both family mixing and CP violation. Therefore, a fourth family would be an unnecessary complication. Singlet heavy neutral leptons are predicted by, for example, left-right symmetric models [44], which constitute electro-weak extensions of the SM. In such models, the big difference between the lepton and neutrino mass scales is explained through the see-saw mechanism [45] by the existence of accompanying heavy right-handed neutrino partners which are weak isospin singlets.

In the case of a doublet, the new leptons would be pair produced in a Z^0 decay, whereas in the case of a singlet, the new lepton could be singly produced with a suppression factor of $|U|^2$ from a Z^0 decay together with a standard lepton [46], where U is the mixing matrix element between the weak isospin singlet and doublet. Here, the flavour diagonality of the Z^0 process is naturally violated. The existence of additional leptons can be restricted either from direct searches after the anticipated signal events or, if their production cross section is sizable, from upper limits on the possible additional Z^0 decay width. In publication I, these two methods are combined to exclude a possible fourth family heavy neutrino with a mass up to almost half the Z^0 mass. The latest LEP measurement of the Z^0 decay width to invisible particles, Γ_{inv} , gives a measurement of the number of light neutrino species of $N_\nu = 2.993 \pm 0.011$ [39].

Repeating the width analysis of publication I using the latest LEP measurements of the total and invisible Z^0 decay width [39], $\Gamma_{\text{tot}}^{\text{new}} = -1.8 \pm 3.1$ MeV and $\Gamma_{\text{inv}}^{\text{new}} = -1.1 \pm 1.8$ MeV are obtained for the additional widths allowed for possible new physics. The new physics widths are negative since the measurements are below the theoretical expectations. Taking a conservative approach and limiting ourselves only to positive new physics widths, $\Gamma_{\text{tot}}^{\text{new}} < 5.0$ MeV and $\Gamma_{\text{inv}}^{\text{new}} < 2.9$ MeV at 95 % CL. The limit on $\Gamma_{\text{tot}}^{\text{new}}$ is valid for any new particle produced in Z^0 decays, whereas the limit on $\Gamma_{\text{inv}}^{\text{new}}$ is valid only for new particles produced in Z^0 decays that escape detection in the experiment. The latter gives a lower bound of 43.1 GeV/ c^2 on the sneutrino mass, if the sneutrino is the lightest supersymmetric particle, using the decay width formula of

Ref. [47]. Converting the limits of new physics widths to lower bounds on the mass of possible new sequential leptons gives: charged lepton heavier than $42.1 \text{ GeV}/c^2$, Dirac neutrino heavier than $45.6 \text{ GeV}/c^2$, stable Majorana neutrino heavier than $44.0 \text{ GeV}/c^2$ and unstable Majorana neutrino heavier than $43.3 \text{ GeV}/c^2$ at 95 % CL. These bounds are somewhat higher than the ones obtained in publication I.

DELPHI has also searched for a singly produced heavy neutrino, ν_L , in Z^0 decays [48] and has excluded any ν_L with a mass between 3.5 and 50 GeV/c^2 if $\text{Br}(Z^0 \rightarrow \nu_L \bar{\nu}) > 1.3 \times 10^{-6}$. Even if it has been proposed that the mixing of right-handed neutrinos with the known neutrinos might reduce the measurable Γ_{inv} [49], additional leptons have to be, in light of the experimental results mentioned above, either heavier than half the Z^0 mass or more or less inert with respect to gauge interactions, having a relative strength of the coupling, $|U|^2$, less than 2×10^{-5} .

2.3 Forbidden Decays

A distinct signal of new physics would be the observation of decays that are forbidden in the SM since they violate some quantum number. For leptons, a very common indicator of new physics would be lepton flavour number violating decays, which are present in many extensions of the SM. A comprehensive review of models containing lepton flavour violation and searches for lepton flavour violation can be found in Ref. [50]. In the case of τ lepton decays are also the so-called second class currents interesting. They have an opposite signed G-parity number compared to the normal weak hadronic current [51] and hence violate G-parity. Baryon number violating decays could also be a subject of study, but indirect bounds coming from proton decay constraints already rule out decays such as $\tau \rightarrow \bar{p} X$ almost completely [52], where X could be any particle(s).

In the minimal SM the lepton family flavour is conserved but in several extensions the lepton family flavour number can be sizably violated, either at the tree-level through mixing of the standard sector with new particles, or at the loop-level through contributions of new particles [53]. The predicted branching ratios of lepton family flavour violating Z^0 decays ranges from $\sim 10^{-4}$ to $\sim 10^{-9}$. In publication II, a search for lepton family flavour violating Z^0 decay was made in the $e\mu$, $e\tau$ and $\mu\tau$ channels. All LEP collaborations have made such searches with negative results [54]. Corresponding

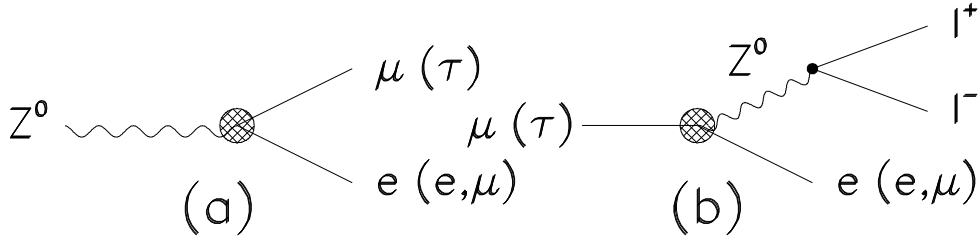


Figure 2: Feynman diagrams for lepton family flavour number violation in (a) Z^0 decays and (b) neutrinoless lepton decays. The shaded circle represents the new physics, which generates the interaction.

Table 4: A comparison of the upper limits obtained at LEP and calculated from neutrinoless lepton decays on lepton family flavour violating Z^0 decays.

Decay	Best LEP limit (at 95 % CL) [54]	Best limit from lepton decay (at 95 % CL) [56]
$Z^0 \rightarrow e \mu$	1.7×10^{-6}	9.7×10^{-13}
$Z^0 \rightarrow e \tau$	7.0×10^{-6}	5.9×10^{-6}
$Z^0 \rightarrow \mu \tau$	9.4×10^{-6}	6.4×10^{-6}

diagrams also give neutrinoless lepton decays with only charged leptons in the final state as is shown in Figure 2 or in the case of the τ lepton, through the axial vector coupling between the light quarks and the Z^0 , the decays $\tau \rightarrow e \pi^0$ and $\tau \rightarrow \mu \pi^0$. The CLEO collaboration has searched for neutrinoless τ decays in a large variety of channels [55]. In Table 4 the limits [56], obtained for neutrinoless lepton decays, are converted into limits on Z^0 decays and compared to the LEP limits [53]. With the exception of the limit on $e\mu$ coming from the measurement $\text{Br}(\mu \rightarrow eee) < 1.0 \times 10^{-12}$ at 90 % CL [56], the LEP limits are competitive. In models with momentum transfer dependent form factors, the direct comparison is not valid anymore and the constraints

from upper limits on neutrinoless lepton decays are much less severe.

In many models, e.g. in supersymmetric ones [57], the tightest constraints on lepton family flavour violation come from the non-observation of radiative charged lepton decays. These decays would arise from one-loop contributions of new particles and, since the general lepton flavour violating lagrangian is non-renormalizable, the limits of the radiative decays cannot be directly compared with the limits given in Table 4 in a model-independent way [53]. The most stringent bounds on radiative lepton decays are at 90 % CL: $\text{Br}(\mu \rightarrow e\gamma) < 4.9 \times 10^{-11}$, $\text{Br}(\tau \rightarrow e\gamma) < 2.7 \times 10^{-6}$ and $\text{Br}(\tau \rightarrow \mu\gamma) < 3.0 \times 10^{-6}$, obtained at LAMPF and CLEO [58]. Radiative τ lepton decays are interesting, though the limit on $\text{Br}(\mu \rightarrow e\gamma)$ is very stringent, since in some superstring inspired models [59], $\tau \rightarrow \mu\gamma$ is enhanced compared to $\mu \rightarrow e\gamma$ by a factor of 2×10^5 . DELPHI has also searched for radiative τ lepton decays [60].

Examples of G-parity violating second class current decays are $\tau \rightarrow a_0(980)\nu_\tau \rightarrow \pi\eta\nu_\tau$ and $\tau \rightarrow b_1(1235)\nu_\tau \rightarrow \pi\omega\nu_\tau$. The theoretical expectation for the $\text{Br}(\tau \rightarrow \pi\eta\nu_\tau)$ is $1.5 \times 10^{-5} \propto |m_u - m_d|^2 / (m_u + m_d)^2$ [61, 62]. Both ALEPH and CLEO [63] have searched for the $\tau \rightarrow \pi\eta\nu_\tau$ decay without success, obtaining an upper limit of 1.4×10^{-4} on the branching ratio. However, they have both observed the equivalent Cabibbo-suppressed decay and measured $\text{Br}(\tau \rightarrow K\eta\nu_\tau) = (2.6 \pm 0.6) \times 10^{-4}$. This decay has no G-parity constraint due to the larger s-quark mass and the theoretical prediction [61, 64] is an order of magnitude higher than for the Cabibbo-allowed decay, in agreement with the measurements.

The measurements of inclusive Cabibbo-suppressed branching ratios, such as $\text{Br}(\tau^\pm \rightarrow K^\pm\nu_\tau \geq 0 \text{ neutrals})$ and $\text{Br}(\tau^\pm \rightarrow K^\pm\nu_\tau \geq 1 \text{ neutrals})$ in publication III, are valuable for the exclusion of the existence of an unexpected decay mode, leading to strange mesons in the final state, having a significant branching ratio. A similar argument holds for the $\text{Br}(\tau^\pm \rightarrow K^\pm K^\mp \pi^\pm \nu_\tau \geq 0 \text{ neutrals})$ measurement of publication IV in the case the unexpected mode would be a Cabibbo-allowed mode. It can be shown [6] that the expected final states saturate the inclusive rates, leaving very little room for additional modes.

3 Experimental Tools and Techniques

3.1 The LEP Collider

The Large Electron Positron (LEP) collider at CERN, the European Laboratory for Particle Physics, situated close to Geneva is currently the world's largest particle accelerator. LEP was commissioned during 1989. In LEP during its first phase, electrons and positrons collide at a center-of-mass (cms) energy, \sqrt{s} , close to the Z^0 mass (~ 91 GeV) with a luminosity of about 10^{31} cm^{-2} s^{-1} [65]. LEP has a circumference of 26.7 km and is situated about 100 m below ground. Four of the interaction regions are equipped with detectors, called ALEPH [66], DELPHI [67], L3 [68] and OPAL [69]. Electrons and positrons enter LEP through a multistage accelerator system with an energy of 20 GeV. In LEP the particles are accelerated by 128 copper radio-frequency field (RF) cavities, which have gradually been replaced by superconducting RF cavities. This has enabled a second phase called LEP2, with a gradual increase of \sqrt{s} , first above the W^+W^- pair production threshold during 1996, and later up to 196 GeV during 1999.

LEP has been an excellent place to measure the characteristics of the Z^0 and its decays due to the increased production rate of Z^0 bosons at the Z^0 resonance. The major achievements of LEP have been to determine the number of light neutrino species to be three and to verify the SM with high precision. Certain extensions of the SM such as the technicolour models [36] are at least very disfavoured by the LEP results compared to supersymmetric models [14]. The major aim of LEP2 is to explore the Higgs sector and measure the characteristics of the W boson.

3.2 The DELPHI Detector

DELPHI is an acronym for DEtector with Lepton, Photon and Hadron Identification. DELPHI [67] is a multipurpose particle detector with a nearly 4π solid angle

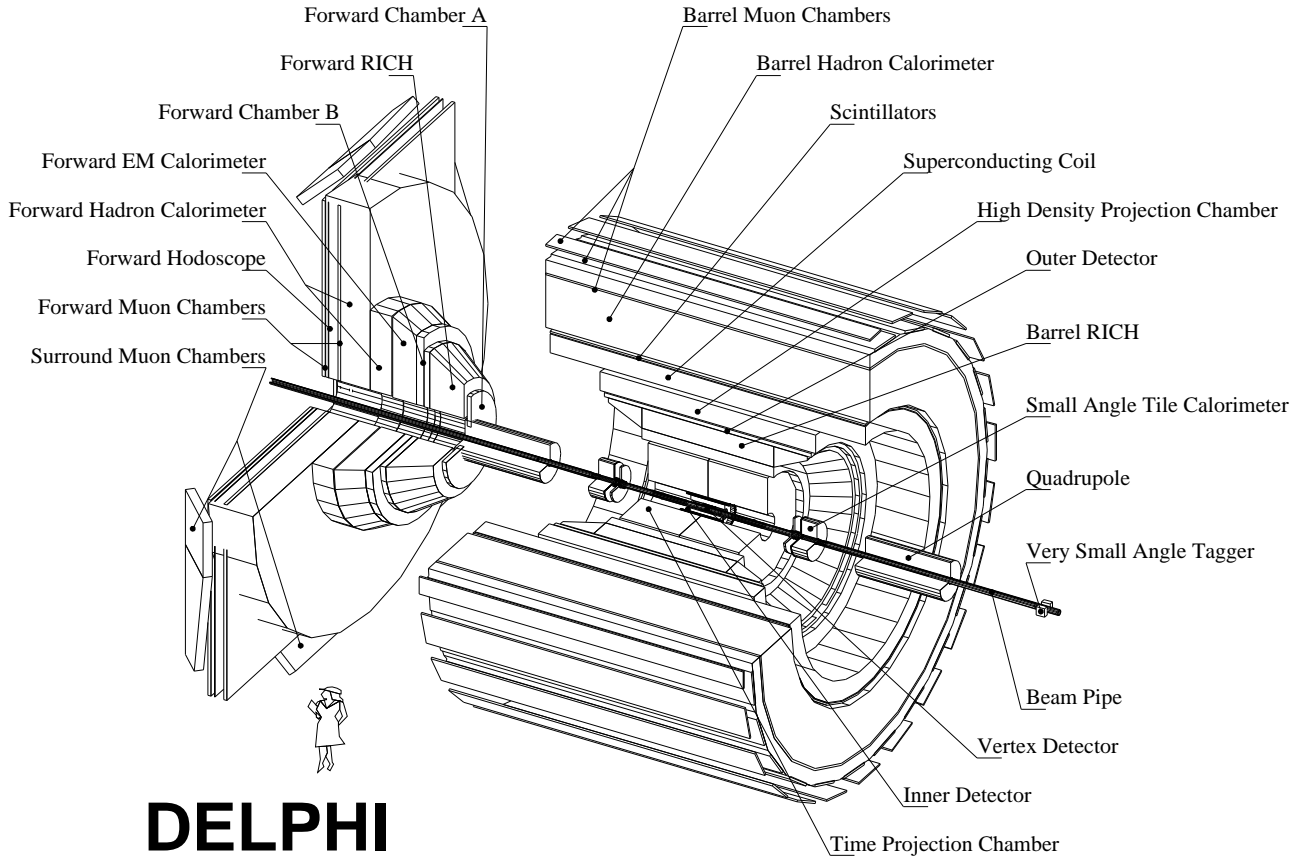


Figure 3: A schematic layout of the DELPHI detector

coverage. Special emphasis has been put on charged hadron identification using Ring Imaging Cherenkov (RICH) counters and on precise vertex determination using silicon microstrip sensors. The detector assembly consists of a cylindrical central region, the so-called barrel, and two endcaps, known as the forward, as seen in Figure 3. A superconducting solenoid, containing the central tracking detectors and the barrel electromagnetic calorimeter, provides a uniform axial field of 1.2 T. A detailed description of the performance of the DELPHI detector can be found in Ref. [70]. In the coordinate system used, the z axis is along the electron direction, the x axis points towards the centre of LEP, and the y axis upwards. The azimuthal angle, ϕ , and the radial coordinate, R , are defined in the $x - y$ plane, and the polar angle, θ , in $R - z$ plane.

3.2.1 Tracking

The primary and secondary vertices of charged particles are determined by the Vertex Detector (VD) [1, 2]. The VD consists of three concentric layers of silicon microstrip sensors at radii of 6.3, 9 and 11 cm covering, before 1996, polar angles of $42^\circ \leq \theta \leq$

138°, where the innermost layer was added for the 1991 data taking. In the initial configuration, the detector provided track coordinates only in $R\phi$, with a measured average resolution of 8 μm . For the 1994 data taking period, the innermost and outermost layers were replaced with double sided sensors to allow measurements in both $R\phi$ and Rz . The innermost layer covers polar angles down to 25° and 155°. In 1996, the polar angular coverage of the other two layers were extended to meet the needs of LEP2 [3]. The VD has an excellent two-track separation of about 220 μm in $R\phi$.

The Inner Detector (ID) [71] immediately surrounds the VD with a polar angle coverage of $30^\circ \leq \theta \leq 150^\circ$. The detector consists of a jet chamber surrounded by five cylindrical layers of Multi Wire Proportional Chambers (MWPC). The jet chamber measures 24 $R\phi$ points per particle trajectory, with a 90 μm point resolution. The MWPC layers provide fast trigger information and a space point measurement in Rz with a resolution of about 600 μm . For the 1995 data taking, the MWPC layers were replaced by five cylindrical layers of straw tube detectors, and the jet chamber by a longer one extending the polar angle coverage to 15° and 165°.

The main tracking device is the Time Projection Chamber (TPC) [72], which is generally used as pivot for the pattern recognition. Both end-plates of the TPC are divided into six azimuthal sectors, each with 192 sense wires and 16 circular pad rows with constant spacing. The TPC thus provides up to 16 space points per particle trajectory at radii of 40 to 110 cm between the polar angles of $39^\circ \leq \theta \leq 141^\circ$. At least three pad rows are crossed by particles with polar angles of $20^\circ \leq \theta \leq 160^\circ$. The single point precision is 250 μm in $R\phi$ and 0.9 mm in Rz . The TPC has a two-track separation of 1.5 cm.

The Outer Detector (OD) [73] consists of five layers of drift tubes, operated in limited streamer mode, located between radii of 197 and 206 cm. The detector provides a fast trigger, and $R\phi$ and Rz point information between polar angles of $42^\circ \leq \theta \leq 138^\circ$. The TPC and the OD essentially provide the information on the position and direction of the particle trajectory inside the Barrel RICH, since the latter is located between the two former, and therefore track information in both the TPC and the OD is crucial for the hadron identification. The position resolution per layer is 110 μm in $R\phi$ and 4.4 mm in Rz . The momentum precision of the barrel is equivalent to

$\sigma(1/P) = 0.6 \times 10^{-3} \text{ (GeV}/c)^{-1}$, if all central tracking detectors are included in the particle trajectory, and degrades whenever one or more is missing.

The Forward Chamber A (FCA), the Forward RICH and the Forward Chamber B (FCB) provide additional tracking information in the endcaps. The momentum precision of the forward is equivalent to $\sigma(1/P) = 1.5 \times 10^{-3} \text{ (GeV}/c)^{-1}$, when at least the FCB is included in the particle trajectory. The trajectory information from the FCB is crucial for the hadron identification with the Forward RICH. The Barrel Muon Chambers (MUB) are the outermost detectors and provide muon identification. The system consists of six planes of drift chambers, two inside the return yoke of the magnet after 90 cm of iron, and four outside after an additional 20 cm of iron. Each chamber has a resolution of 2-3 mm in $R\phi$ and about 2.5 cm in Rz . The polar angle acceptance of the system is $53^\circ \leq \theta \leq 127^\circ$. A similar system, The Forward Muon Chambers (MUF), provide muon identification in both endcaps.

3.2.2 Luminosity Measurement and Calorimetry

The luminosity is measured by counting the number of Bhabha scattering events, $e^+e^- \rightarrow e^+e^-$ at small polar angles, where the scattering is dominated by a t-channel photon exchange. The process has a high cross section and the cross section has been theoretically calculated to a very high precision. In DELPHI, before 1994, the measurement was performed using the Small Angle Tagger (SAT), formed by two cylindrical detectors placed around the beam pipe on either side of the interaction region. The SAT consisted of a tracker part in front of a calorimeter with alternating lead sheets and scintillating fibers. In 1994, the SAT was replaced by the Small angle Tile Calorimeter (STIC) [74], a sampling lead-scintillator calorimeter built with the shashlik technique. The polar angular acceptance was increased from 43-135 mrad to 29-185 mrad.

The Very Small Angle Tagger (VSAT) [75] is located further from the interaction region along the beam pipe. This calorimeter consists of four rectangular modules, with alternating tungsten absorber layers and silicon sensors, placed horizontally on both sides of the beam pipe. The task of the VSAT is to measure the relative luminosity of each cms energy. The polar angle acceptance is 4-8 mrad for an azimuthal coverage of $\pm 45^\circ$ around the horizontal axis. A precise luminosity measurement is essential for

the electroweak precision measurements, and up to now a precision of 0.09 % [39] has been achieved.

The barrel electromagnetic calorimeter of DELPHI is a High-density Projection Chamber (HPC) [76]. The HPC is a sampling calorimeter using the time projection principle, with alternating lead converter layers and drift channels. The charge created by a shower is read out by a proportional wire plane at the end of each module, giving a three dimensional charge distribution of the shower, with high granularity. The precise imaging of the shower development allows discrimination of electrons and photons against hadrons, and the identification of π^0 mesons which decay into two nearly parallel photons. The HPC covers polar angles of $43^\circ \leq \theta \leq 137^\circ$ with an energy resolution of $\sigma(E)/E = (32/\sqrt{E} \oplus 4.3) \%$ (E in GeV). The angular precision of the reconstructed shower for high energy photons is 2 mrad in ϕ and 1 mrad in θ . The Forward Electromagnetic Calorimeter (FEMC) consists of lead blocks and has a 5 % energy resolution at 45 GeV.

The Hadron Calorimeter (HCAL) [77] is a sampling calorimeter embedded in the magnet yoke with alternating iron plates and gas detectors working in limited streamer mode. It consists of barrel and forward parts with some angular overlap, where the total polar angle coverage is $11^\circ \leq \theta \leq 169^\circ$. The energy resolution in the barrel is $\sigma(E)/E = (112/\sqrt{E} \oplus 21) \%$ (E in GeV), where the fixed term is essentially due to the material in front of the hadron calorimeter.

3.2.3 Trigger and Data Acquisition System

The aim of the trigger is to filter interesting events from background events. The DELPHI trigger scheme consists of four trigger levels, reducing the collision rate of 45 or 90 kHz, corresponding to four or eight bunches of electrons and positrons per beam, to a data recording rate of a few Hz. The first two levels are hardwired combinations of trigger signals from the subdetectors, operating synchronously with the Beam Cross Over (BCO) signal. The third level trigger is a software trigger with some reconstruction running asynchronously with the BCO. An additional fourth level software trigger exists, with the capability of fully reconstructing the event and has been utilized since 1994, to reduce the amount of background events recorded by a factor two.

In addition to the detectors mentioned before, DELPHI contains a few detectors specialized in triggering, namely the scintillators embedded in the HPC, the Time-Of-Flight (TOF) and the Forward Hodoscope (HOF). They all consist of scintillators giving fast trigger signals. For eight bunches, the first level and second level decisions are taken $3.5 \mu\text{s}$ and $39 \mu\text{s}$ after the BCO, introducing a dead-time of about 3 %. At present, 17 decision functions exist, which combine the triggers from subdetectors, providing substantial redundancy. The trigger efficiency is practically one for events with charged particles with polar angles of $20^\circ \leq \theta \leq 160^\circ$.

The DELPHI Data Acquisition System (DAS) is based on the FASTBUS standard [78]. The DAS is built in a treelike structure with the global control and transfer system, the so-called central partition, on the top, and the partitions of the subdetectors as branches. The trigger has its own partition. The front-end unit of each partition runs synchronously with the BCO converting the analogue data to digital form. The digitalized data is filled in one slot of a four-event buffer and the data filling is switched to the next slot after a second level trigger acceptance.

The operations within a partition and the readout of a partition is handled by software running in a Fastbus Intersegment Processor (FIP) unit. A Local Event Supervisor (LES) software process performs the readout and builds the data structure for each partition, whereas a Global Event Supervisor (GES) software process, running in a central partition FIP, builds up the data structure for the whole event only when the event has been accepted by the third level trigger. Each subdetector has the possibility to monitor its own data in the LES. The recorded data is processed instantly through the DELPHI Reconstruction program (DELANA) [79], giving immediate feedback on the quality of the data and performance of each subdetector. The average efficiency of the DAS is about 85 %, where half the dead time is due to recovery time after DAS crashes. The average hadronic Z^0 event size is about 150 kbytes.

3.2.4 The Ring Imaging Cherenkov Detectors

The charged hadron identification in DELPHI is based on using the Ring Imaging Cherenkov (RICH) technique. The development of RICH detectors was initiated by Seguinot and Ypsilantis [80] and is based on the measurement of the emitted Cherenkov

radiation from ultra relativistic particles. The RICH system in DELPHI comprises of the Barrel RICH (BRICH) [81] in the central region and two endcap detectors, which together form the Forward RICH (FRICH) [82]. The identification is complemented by the specific ionization (dE/dx) in the TPC. The resolution of the dE/dx is 5 % in a single particle environment and degrades to 7 % in a hadronic Z^0 environment.

Charged particles moving through a transparent dielectric medium with a velocity, v , larger than the phase velocity of light in that medium ($= c/n$, where n is the refractive index of the medium) emit radiation under a specific angle with respect to the direction of flight. The angle between the propagation direction of the particle and the emitted radiation, the so-called Cherenkov angle, θ_C , is given by:

$$\cos \theta_C = \frac{1}{\beta n} = \frac{\sqrt{1 + m^2/P^2}}{n}, \quad (33)$$

where m and P are the mass and momentum of the particle and $\beta = v/c$. Therefore, the velocity of a particle can be determined by measuring the Cherenkov angle. Since the momentum is known from the tracking detectors, the mass can be determined and the particle is, consequently, identified.

For a particle path length, l , in the radiator medium, the number of detected photons, n_{ph} , is $n_0 l \sin^2 \theta_C$, where n_0 is a quality factor taking into account the various multiplicative efficiency factors of the actual detection medium, such as the quantum efficiency of the photon conversion mechanism, the mirror reflectivity and inefficiencies in the detection of the photo-electrons produced. Below the threshold velocity, $\beta_{th} = 1/n$, no photons are emitted and slightly above threshold, the Cherenkov angle is small. The Cherenkov angle and number of emitted photons increase with increasing β , until β approaches one, where the Cherenkov angle is at its saturated value, $\theta_C^{sat} = \arccos(1/n)$, and the number of emitted photons reaches its plateau value.

The principle of operation of the DELPHI RICHes is illustrated in Figure 4. A charged particle traverses both a liquid and a gas radiator with an ultraviolet (UV) photon detector in between. The Cherenkov photons produced in the liquid radiator are converted in the UV photon detector and form a ring around the specific ionization left by the particle. The Cherenkov photons produced in the gas radiator are projected back by parabolic mirrors, positioned at the exit of the whole detector system, to the UV photon detector. The ring formed by these photons will be displaced with respect

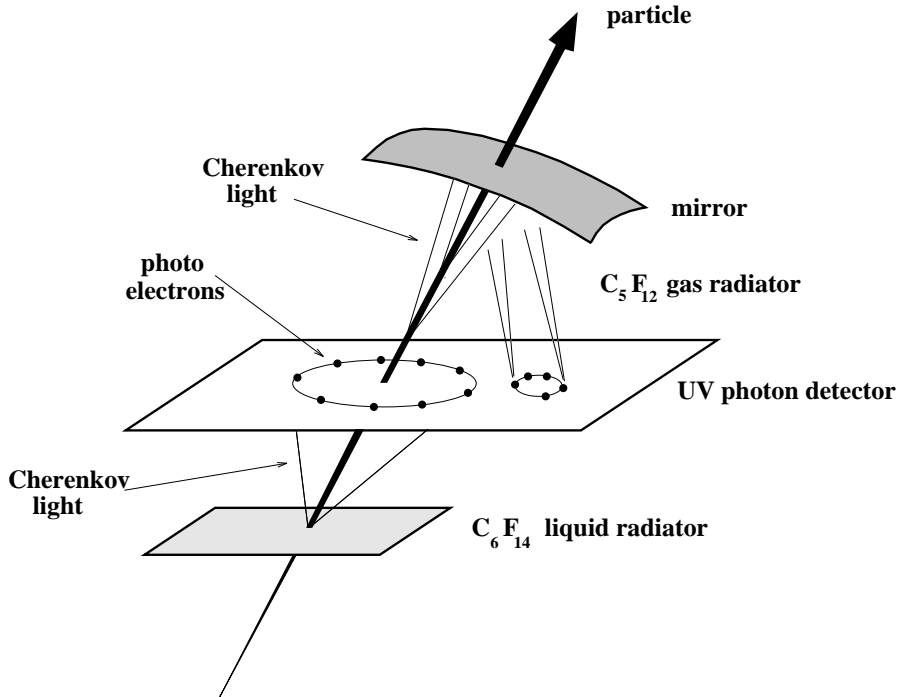


Figure 4: The operation principle of the RICH

to the particle trajectory and will have a considerably smaller radius than the ring from the liquid Cherenkov photons. The liquid and gas Cherenkov photons can also be distinguished by their conversion depth in the UV photon detector.

In DELPHI, liquid and gaseous radiator media are used in order to enlarge the momentum range over which particles can be identified. The selected radiator substances are all perfluorocarbons. Perfluorohexane, C_6F_{14} , is used as liquid radiator for both RICHes, while the gas radiators are perfluoropentane, C_5F_{12} , and perfluorobutane, C_4F_{10} , in the Barrel and Forward RICH, respectively. Some of the properties are given in Table 5. The gas radiator is used for high momentum particles and the liquid radiator for low momentum particles. Figure 5 shows the Cherenkov angle as a function of the particle momentum for different types of particles, both in gas and liquid radiators. The power of the particle identification is determined by the separation between the particle bands in Figure 5 in units of the resolution of the Cherenkov angle. Kaons produced in τ decays at the Z^0 pole have momenta above $3.5 \text{ GeV}/c$, where the Cherenkov angle of the liquid radiator is already saturated. Therefore in this thesis the main focus will be on the gas radiator and on its K/π separation capability.

The BRICH is a 3.5 m long cylinder with inner and outer radii of 130 and 197

Table 5: Properties of radiators [83]

Radiator medium	C_4F_{10}	C_5F_{12}	C_6F_{14}
Boiling temperature ($^{\circ}C$)	- 2	28	57
Refractive index (at 7 eV)	1.00155	1.00172	1.283
Threshold for kaon (GeV/c)	9.0	8.3	0.62

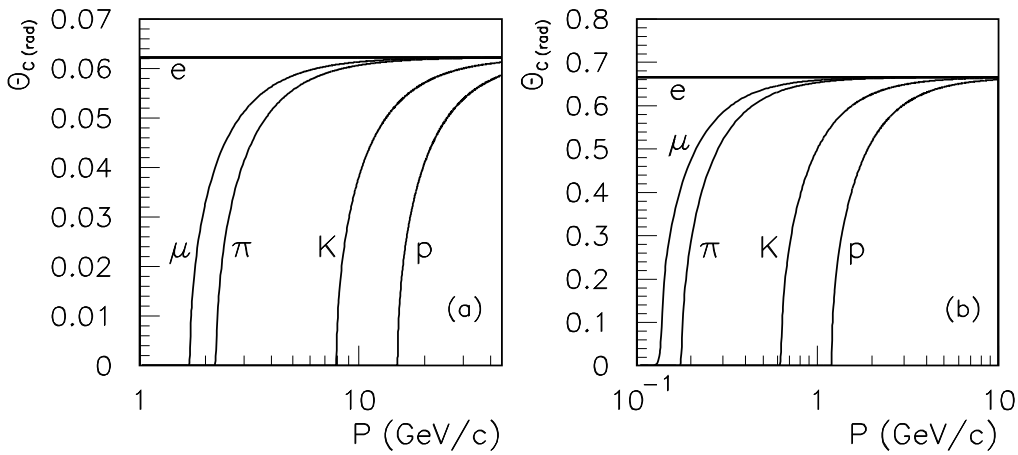


Figure 5: Cherenkov angle in the Barrel RICH as a function of particle momentum for electrons (e), muons (μ), pions (π), kaons (K) and protons (p), (a) in the gas radiator C_5F_{12} and (b) in the liquid radiator C_6F_{14} .

cm , respectively. A mid-wall divides the detector into two identical halves, referred to as sides A and C. The polar angle coverage of the detector is $40^{\circ} \leq \theta \leq 140^{\circ}$. Each side of the BRICH is azimuthally divided into 24 sectors. The elements of a sector are one liquid radiator, one drift tube with a wire chamber at its end and six mirrors. An undivided gas radiator volume is common to all sectors. The liquid radiator consists of a 1 cm thick layer of C_6F_{14} . The whole vessel is filled with the gaseous radiator C_5F_{12} and the average path length of particles in the gas volume is 40 cm.

A set of drift tubes forms the UV photon detector of the BRICH. The tubes are constructed from UV grade quartz plates and contain a gas mixture of 75 % CH_4 and

25 % C₂H₆. The drift gas is made photosensitive by bubbling through liquid TMAE¹, which has an ionization potential of 5.4 eV. A drift field transports the photo-electrons towards a MWPC at the end of the drift tube. Each MWPC has 196 anode wires at 2.62 mm pitch and 196 cathode pads at 4 mm pitch. Photo-conversion points are reconstructed in three dimensions. The anode wire address provides the $R\phi$ coordinate and the cathode pad address the R coordinate. The z coordinate is determined by the drift time. Combined with the particle trajectory measured by the tracking detectors, the Cherenkov angle can be calculated for each photon.

The BRICH started operating during the 1991 data taking period and has been fully operational since the 1992 data taking period. The performance figures for the BRICH for muon pairs at 45.6 GeV are: in the liquid and gas radiators the number of photons per ring are 14 and 8; per individual photon, the resolution of the Cherenkov angle is 13.3 and 4.3 mrad, with the saturated angle 666 and 62.3 mrad, respectively.

The FRICH covers both end-cap regions of DELPHI over polar angles $15^\circ \leq \theta \leq 35^\circ$ and $145^\circ \leq \theta \leq 165^\circ$. Although very different in geometry, it employs the same principle as the BRICH. The FRICH has been fully operational from the 1994 data taking period onwards. The performance figures for the FRICH for muon pairs at 45.6 GeV are: in the liquid and gas radiators the number of photons per ring are 7 and 8; per individual photon, the resolution of the Cherenkov angle is 11.4 and 2.5 mrad, with the saturated angle 675 and 55 mrad, respectively.

3.3 Charged Kaon Identification

In this section some of the experimental issues on charged kaon identification with the RICH are elaborated upon. As already mentioned, the charged hadron identification in DELPHI is based on the RICH and complemented by the specific ionization (dE/dx) in the TPC. Due to the better particle separation in the RICH, the RICH identification is better suited for an analysis, in which high rejection power and exclusive particle tag is desired, whereas particle identification using the dE/dx measurement is more adjusted to an analysis, in which more moderate rejection power and perhaps a statistical tag

¹Tetrakis(dimethyleamino)-ethylene

is sufficient. In τ decays, for example, a rejection power of 20 or more is necessary to remove the background sufficiently [84] and therefore the RICH is used, while on the contrary, for high momentum particles from heavy quark decays a rejection power of five is adequate [85], and therefore a combination of RICH and TPC can be used to obtain a high efficiency. Since we are interested in separating kaons from pions in τ decays here, only the RICH has been used for the identification. The FRICH was not included in any of the τ analyses due to the poor tracking quality and lower statistics in the forward region.

The branching ratios of Cabibbo-suppressed τ decays have also been determined by ALEPH [8,86] and CLEO [87], using their dE/dx measurements for kaon identification. ALEPH performed a statistical fit of the hadron fractions in the x_π distribution, where $x_\pi = (dE/dx_{\text{meas}} - dE/dx_{\text{exp},\pi}) / \sigma_{dE/dx}$, using the expected x_π functions for pions and kaons, whereas CLEO selected kaon candidates on event-by-event basis, based on the compatibility of the dE/dx and TOF measurements with the kaon hypothesis.

The kaons from τ decays at LEP have momenta above 3.5 GeV/ c . The Cherenkov angle in the liquid radiator is already saturated for these momenta as shown in Figure 5. Therefore, only the data from the gas radiator has been used. Two techniques are used for identifying the kaons. Up to ~ 9 GeV/ c , kaons are below the threshold for producing Cherenkov photons, while pions yield saturated angles, hence in this region the kaons are identified by specifying that no photons ² were attributed to the particle ("veto identification"). Above the kaon threshold of ~ 9 GeV/ c , the kaons are identified using the Cherenkov angle determined from the detected Cherenkov photons ("ring identification") up to ~ 22 GeV/ c . For higher momenta, the difference between the expected Cherenkov angle for a kaon and a pion is too small, as can be seen from Figure 5, to be able to separate them with the experimental precision achieved.

3.3.1 Determination of the Cherenkov Angle and its Error

The stability and behaviour of the RICH was studied using muons from the decay $Z^0 \rightarrow \mu^+\mu^-$, which is a clean sample of particles for which the Cherenkov angle is always saturated. Bad runs and modules were identified and removed from further

²For convenience the word 'photon' is used instead of the more accurate term 'photo-electron'.

analysis if the fraction of muons giving a low number of photons was large. Using the same muons, the Cherenkov angles of individual photons were corrected for effects due to mirror misalignments. The uncertainty of the Cherenkov angle determination from individual photons, σ_γ , has contributions from several sources. For the photons from the gas radiator:

$$\sigma_\gamma^2 = \sigma_{\text{chrom}}^2 + \sigma_{\text{bend}}^2 + \sigma_{\text{position}}^2, \quad (34)$$

where σ_{chrom} is the error due to chromatic aberration, i.e. the variation of the refractive index with photon energy, which is in the order of a few %. The term σ_{bend} is caused by the bending of the particle trajectory in the 1.2 T magnetic field of DELPHI, which smears the Cherenkov angle in one direction. Finally, σ_{position} is the measurement error of the photon position, which includes diffusion during the drift of the photo-electrons and the intrinsic resolution of the wire chamber, which detect the photo-electrons at the endplates of the UV photon detectors.

At muon momenta of 45 GeV/c, σ_γ is dominated by σ_{position} and therefore effects due to residual misalignment, drift diffusion and distortions can be parameterized and included in σ_γ as a scaling. Residual z misalignment between the BRICH and the TPC, for example, leads to a shift of the reconstructed particle path in BRICH with respect to the true trajectory. This is seen as an apparent degradation of the Cherenkov angle resolution that depends on the azimuthal position (ϕ_C) of the photon along the ring image. The size of the effect is also dependent on the drift distance and thereby mirror dependent. To cure this and other residual drift effects, σ_γ was scaled for each mirror group with a constant term and another term depending on $\cos \phi_C$ in order to have a resolution function, defined as the difference between the measured and expected Cherenkov angle divided by the expected error, with a width of one.

For the determination of the average Cherenkov angle ($\bar{\theta}_C$) [88], the photons were grouped into clusters of a similar angle. For each cluster, $\bar{\theta}_C$ was calculated as the weighted average of all photons in the cluster, with a weight equal to a^2/σ_γ^2 . The factor a for a certain class of photons was set taking into account the signal to background ratio since, for example, the background is higher for ambiguous photons, i.e. photons being attributed to more than one particle, than for unambiguous photons. The background is due to feedback photons, cross talk between wires, rings belonging to other particles

and ionization caused by the particles when they pass through the photon detector.

Photons with an individual Cherenkov angle within a $2.5\sigma_\gamma$ window around $\bar{\theta}_C$ were kept in a cluster. In an iterative procedure using this criterion, background hits were removed and new photons were allowed to be included into the cluster. The cluster with the highest number of weighted photons was selected, the weight of a photon being the factor a mentioned previously. In the second step, the ambiguities between the main cluster for each particle were solved. Ambiguous photons that were used only in one main cluster were attributed to the corresponding particles as unambiguous. The remaining ambiguities could be classified as gas-gas or gas-liquid ambiguities. The latter could be resolved by comparing the conversion probabilities based on the conversion depth, since the liquid photons are emitted before the photon detector, whereas the gas photons are reflected back to the photon detector. For the former, a decision was taken on the basis of the number of unambiguous photons in both clusters and the χ^2 contribution of the photon to each ring. After solving ambiguities, a final iteration was made to obtain the average Cherenkov angle and its error.

3.3.2 Kaons in τ Decays

During recent years there has been a growing interest in measuring the decays of the τ lepton into strange mesons. In addition to decay modes involving charged kaons, decay modes with K_L^0 's and K_S^0 's have been measured [6]. K_L^0 's are identified by their shower in the hadron calorimeter, whereas K_S^0 decays into two charged pions are recognized by finding a two charged particle vertex, which is clearly separated from the interaction point. The measurement of these decay modes have improved the understanding of the formation of resonant hadronic states in τ decays.

Furthermore, the modes with three charged particles in the final state (three “prongs”): $\tau^\pm \rightarrow K^\pm K^\pm \pi^\pm \nu_\tau$ (neutrals) and $\tau^\pm \rightarrow K^\pm \pi^\pm \pi^\pm \nu_\tau$ (neutrals), where (neutrals) denotes inclusion of modes with additional neutral hadrons, could be used for studies of a possible ν_τ mass, if sizable samples with small backgrounds could be extracted. This was, however, not achieved with the analysis in publication IV. Further improvements would have to be made to reduce the probability of a pion being identified as a kaon in order to be competitive with the analysis of the three and five

prongs [89]. Due to the boost the τ receives in the Z^0 decay, the final state particles in the three prong decay traverse DELPHI close together, as can be seen from Figure 6. This means that the images of the Cherenkov rings in BRICH may overlap, so that many of the photons may be attributed to more than one particle. To get a good K/ π separation, the ambiguous photons have to be attributed to the correct particles. Hence the rejection power achieved in publication IV was not as good as in publication III. The achieved rejection power of about 20 was not sufficient for a $\text{Br}(\tau^\pm \rightarrow \text{K}^\pm \pi^\pm \pi^\pm \nu_\tau (\text{neutrals}))$ measurement.

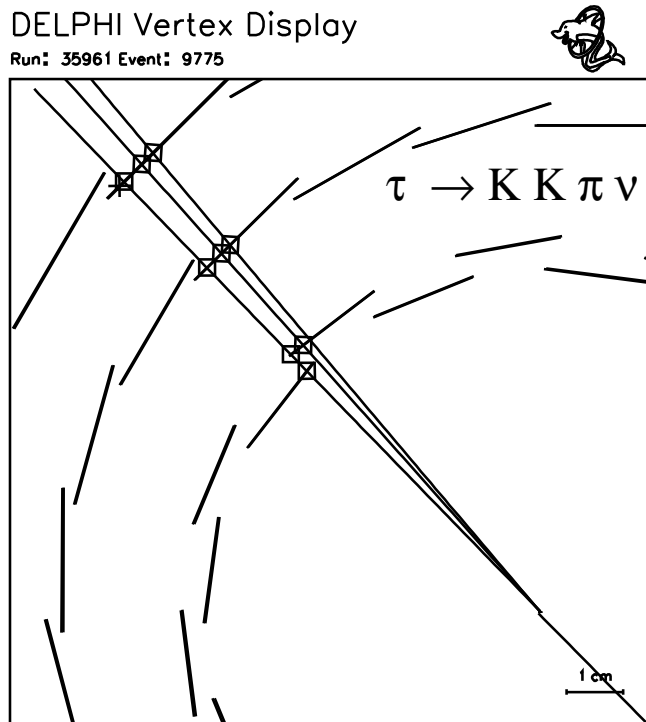
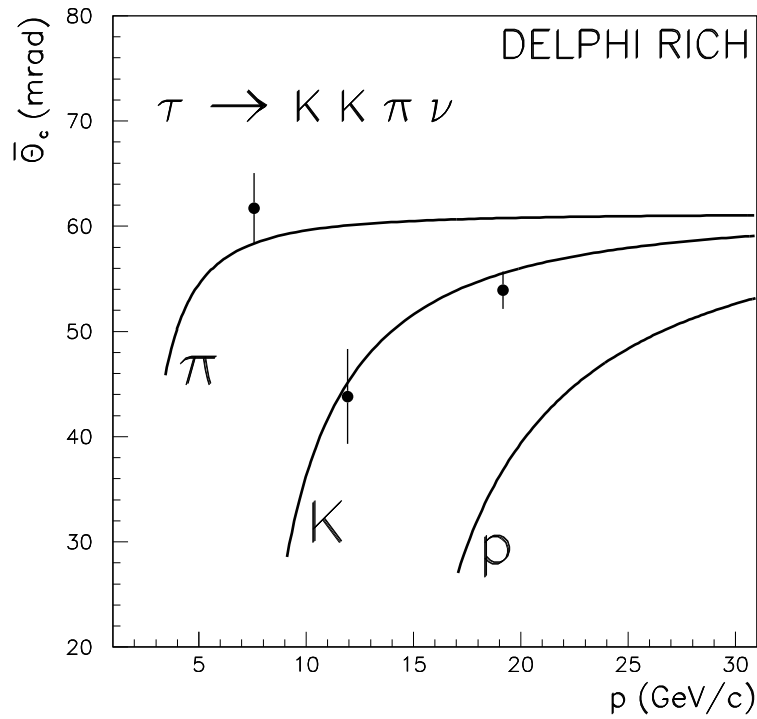


Figure 6: A $\tau^\pm \rightarrow K^\pm K^\mp \pi^\pm \nu_\tau$ candidate event with unambiguous RICH hadron identification (upper) as seen in the $R\phi$ plane of the Vertex Detector (VD) (lower). The lines in the upper plot are the expected Cherenkov angles for different hadron species and the squares in the lower plot are the associated VD clusters.

4 Silicon Vertex Detectors

4.1 Design Considerations

The physics motivation of a high precision vertex detector is to improve the charged particle reconstruction close to the interaction point. This is crucial for studies of decay vertices of long lived particles, such as B flavoured hadrons or τ leptons. The presence of a long lived particle can either be detected based on reconstruction of a secondary vertex, i.e. a separate vertex of particles, which is incompatible with the interaction point, or based on individual impact parameters, the distance of closest approach from a particle to the interaction point. The sign of the impact parameter is defined with respect to the jet direction so that it is positive if the vector joining the primary vertex to the point of closest approach of the track is less than 90° from the direction of the jet to which the particle belongs. The interaction point can either be determined directly on the same event as a primary vertex based on the hadronization particles, or as an average of the primary vertices of events, adjacent in time with the studied event.

A measure of the quality of a vertex detector is the error of the impact parameter, σ_{IP} , which is a combination of the error of the extrapolation to the interaction point and the uncertainty of the knowledge of the primary interaction point, σ_{PV} . The error of the impact parameter is given by

$$\sigma_{IP}^2 = \sigma_0^2 + \sigma_{MS}^2 + \sigma_{PV}^2, \quad (35)$$

where σ_0 is the uncertainty of the extrapolation due to detector resolution and geometry and σ_{MS} is the uncertainty of the extrapolation due to multiple scattering. Two points measured with high precision are enough to obtain a satisfactory small σ_{IP} , but typical sensors have defects that decrease the detection efficiency, so for a vertex detector with only two sensor layers, a fraction of particles will have only one high precision point. Therefore, in DELPHI a third sensor layer was added to increase the redundancy and also to assist in the alignment procedure.

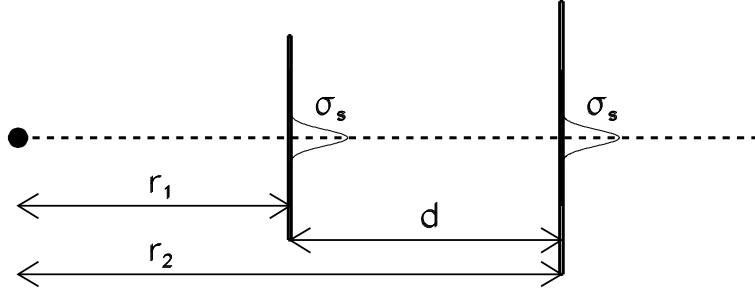


Figure 7: A sketch of a two layer vertex detector.

The expression for the extrapolation error to the origin for a particle traversing through two sensor layers with sensor resolutions, σ_s , at distances r_1 and r_2 from the interaction point can be approximated by

$$\sigma_0 = \frac{\sigma_s}{d} \sqrt{r_1^2 + r_2^2}, \quad (36)$$

if the multiple scattering is neglected i.e. the transverse momentum is very large. d is the lever arm as shown in Figure 7. In order to have a small σ_0 , it is obvious that the lever arm should be long or the distance of the sensor layers to the interaction point short and the sensor resolution as good as possible. Usually the two former are very difficult to optimize since the lever arm is limited by the space between the beam pipe and the main tracking chambers. Also, the distance between the first measurement and the interaction point is limited by the radius of the beam pipe and the radiation tolerance of the sensors and the electronics, which are both dependent on the beam backgrounds in the collider. Therefore, a good resolution, i.e. small σ_s , is crucial.

At transverse momenta of a few GeV/ c , typical of B decay products, the multiple scattering in the material already gives a larger contribution to the extrapolation error than resolution and geometry. The leading term of the multiple scattering error is proportional to $\sqrt{x/X_0}/P_T$ [90], where x is the length of material traversed, X_0 is a material dependent radiation length constant and P_T is the transverse momentum. Since in a barrel geometry $\sqrt{x} = \sqrt{x_T/\sin\theta}$, where x_T is the thickness of the material, and $P_T = P \sin\theta$, σ_{MS} can be approximated by

$$\sigma_{MS} = \frac{\alpha_{MS}}{P \sin^{3/2}\theta}. \quad (37)$$

α_{MS} is a detector dependent multiple scattering coefficient in units of $\text{GeV}/c \cdot \mu\text{m}$, P is the particle momentum and θ is the polar angle. The size of α_{MS} depends on the type and amount of material in the beam pipe and in the sensor layers. In order for α_{MS} to be small, the materials in the beam pipe and sensor layers should be minimized and be selected by taking their X_0 into account. The uncertainty of the knowledge of the primary interaction point, σ_{PV} , is dependent on, in addition to the extrapolation error, the size and the stability of the beams in the collider.

4.2 The DELPHI Vertex Detector

At LEP all vertex detectors were chosen to be small size assemblies of silicon microstrip sensors due to the high reliability, high efficiency and good resolution. The DELPHI Vertex Detector (VD) consists of three concentric layers of sensors at radii of 6.3, 9 and 11 cm, covering polar angles of about $42^\circ \leq \theta \leq 138^\circ$. As can be seen from the schematic layout of the 1994-95 detector in Figure 8, each layer consists of 24 ladders in a staggered design and each ladder consists of four silicon microstrip sensors mechanically attached together.

The VD has undergone three major upgrades since the first installation of a complete two layer detector with single sided sensors having $R\phi$ -readout in spring 1990 [1]. The first upgrade became possible in 1991, after the reduction of the LEP beam pipe radius, allowing a third single sided layer to be added to the existing configuration at a significantly smaller radius [1]. In 1994, the detector was upgraded by replacing two layers with double sided sensors having both $R\phi$ - and Rz -readout [2] and hence the efficiency of the reconstruction and the identification of long lived particles could be improved by means of high precision three dimensional tracking. The third upgrade of the detector, extending the coverage of the detector by doubling the length of the barrel and mounting small silicon trackers as endcaps on each end, was installed for the 1996 data taking [3]. This upgrade was made to meet the needs of LEP2 with a larger fraction of jets occurring in the forward regions due to more events with a four fermion final state, and a necessity to extend the b-tagging capability to larger values of $\cos \theta$ for Higgs and supersymmetric particle searches.

In DELPHI, special care has been taken to minimize the material, for example, by

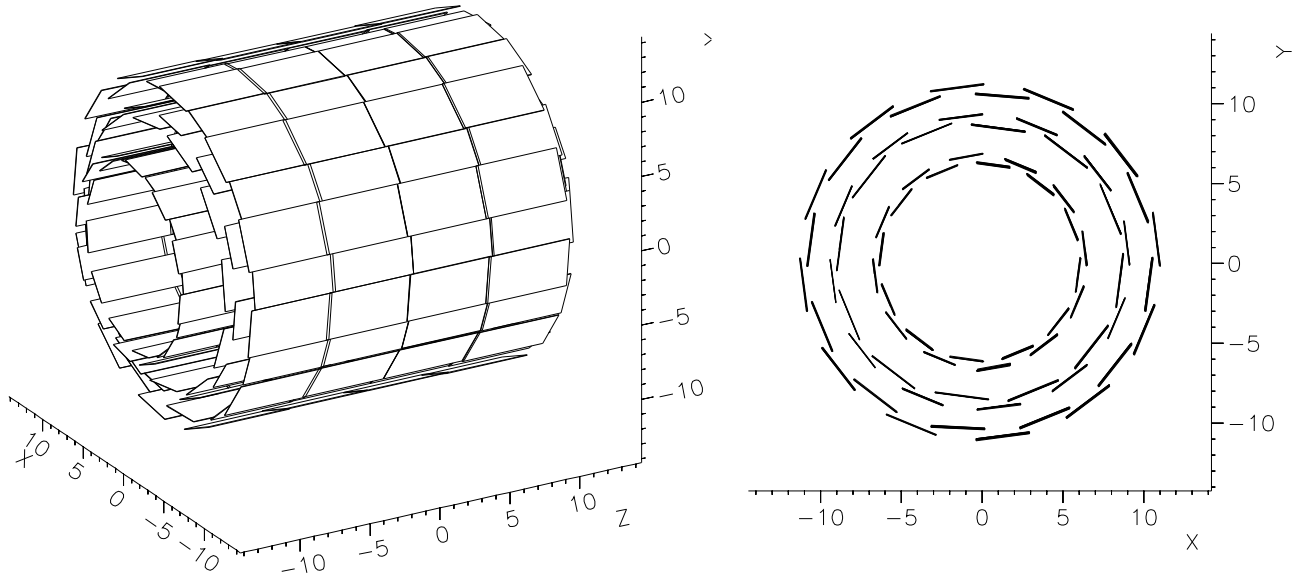


Figure 8: A schematic layout of the 1994-95 DELPHI Vertex Detector (scale in cm). The detector is shown in perspective view in the left drawing and in the view transverse to the beam pipe in the right drawing.

using double sided double metal sensors. Furthermore, the resolution in Rz has been optimized by varying the distance between the strips³ on the sensor as a function of θ in order avoid the charge being spread over too many implants and hence degrade the resolution dramatically at larger values of $\cos\theta$. The sensor resolution for the 1994-95 detector in $R\phi$ was about $8\ \mu\text{m}$ and in Rz at best $9\ \mu\text{m}$ at $\theta = 90^\circ$ with a slow degradation of the resolution as a function of θ . The impact parameter resolution obtained in $R\phi$, when σ_{PV} has been subtracted, corresponds to a σ_0 of $20\ \mu\text{m}$ and a σ_{MS} of $65\ \mu\text{m}$. If the degradation of sensor resolution as a function of θ is parameterized by an additional factor $1/\sin\theta$ in both terms of (35), the impact parameter resolution in Rz could be parameterized with a σ_0 of $39\ \mu\text{m}$ and a σ_{MS} of $71\ \mu\text{m}$ [2].

4.2.1 Sensors

The most important components of vertex detectors are the sensors and the electronics with high density packing of readout channels, which make precise position resolution possible. The production of silicon sensors by planar technology, originally developed

³For convenience the word 'strip' is used instead of the more accurate term 'strip implant'.

for the processing of integrated electronics, was introduced in 1980 [91] and allowed processing of densely packed sensor elements. A typical silicon microstrip detector, as shown in Figure 9, has ion implanted or diffused p^+ -doped strips on the junction side (the so-called p-side) of a high resistivity n-type silicon bulk. The strips are surrounded by a bias line and a p^+ -doped guard ring structure. Single sided silicon sensors have a uniform n^+ -doping on the ohmic side (known as the n-side). The readout lines are aluminized on top of the p^+ -strips with a thin coupling oxide in between, functioning as a coupling capacitor [92]. The biasing voltage is applied to the strips through individual polysilicon resistors as shown in Figure 9. The polysilicon resistors are directly processed onto the sensors with both the strips and the biasing line connected to the resistors through contact holes [1].

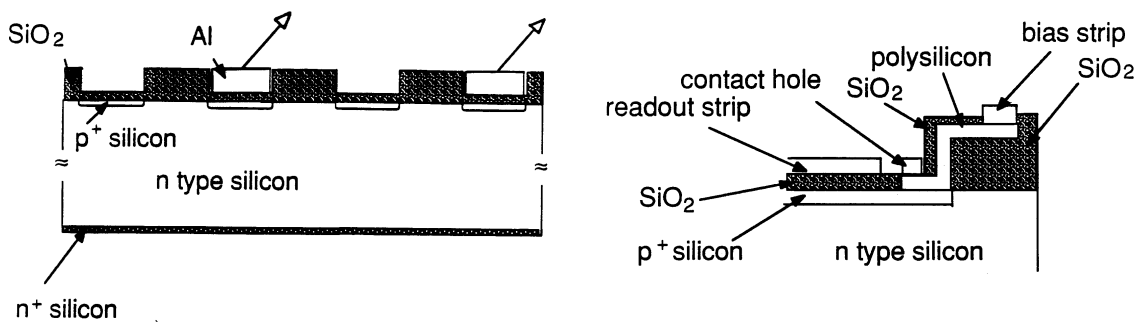


Figure 9: Cross section of a sensor (left drawing) and a strip of a sensor (right drawing) with integrated coupling capacitors and biasing resistors.

A method of reducing the number of readout channels without reducing the good position resolution is to leave “floating” strips not connected to electronics between the strips read out. The charge deposited between strips is capacitively coupled to the closest strip, but then the floating strip will capacitively couple an equal amount of the charge to the neighbouring strips, which are read out. The DELPHI sensors have strips spaced every $25 \mu m$ for the $R\phi$ -readout, but only every second strip has a readout line as shown in Figure 9. The thickness of the sensors is about $300 \mu m$.

In order to obtain two dimensional position information with a sensor, processing has to be done on both sides. The processing of n^+ -strips on the n-side is difficult because of a natural accumulation of electrons at the Si- SiO_2 interface. This electron layer leads to lower interstrip resistances and that in turn results in a sharing of the

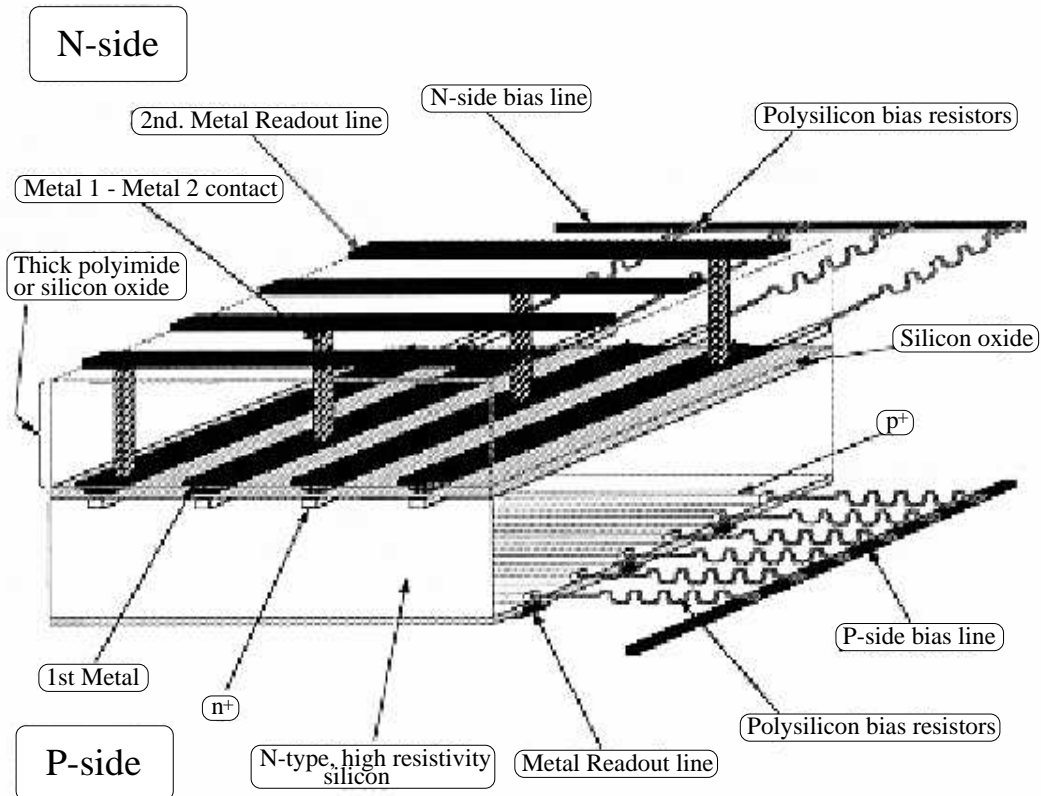


Figure 10: Cross-sectional view of a complete double sided double metal sensor with field plate separation of the n^+ -strips.

produced charges over many strips. The solution is to disrupt the electron layer either by introducing blocking p^+ -doping between the n^+ -strips or using the metal readout lines with enlarged width as field plates over the strips to create a field to repel the electrons [2]. Both techniques were used for the double sided sensors of DELPHI.

The strips perpendicular to the beam create an additional problem, when the aim is to minimize the multiple scattering, since the signals have to be rerouted somehow to either end of the barrel in order not to have additional material in the form of electronics, where most of the particles traverse. Therefore, DELPHI decided to develop a double metal process, where the routing lines are integrated on the sensor itself as shown in Figure 10. The first metallization layer capacitively couples the n^+ -strips and the second metallization layer, perpendicular to the first one, routes the signals to the end of the barrel. The process requires a thick layer ($\sim 5 \mu\text{m}$) of insulator made either of polyimide or silicon oxide between the metal layers. In the insulator, contacts are opened to have the desired connections between the metal layers. These sensors are much more complicated to produce than single sided sensors. Therefore, studies of the

long term behaviour were made and severe acceptance tests were applied to ensure the reliability of the sensors used in the experiment [2].

The optimal resolution of a vertex detector cannot be obtained without a thorough knowledge of the exact geometry and position of each sensor. The process to determine this is called alignment and already starts when the detector is being built. The detector parts are made with a mechanical accuracy of about $20\ \mu\text{m}$ to avoid mechanical stress in the assembly. In the mounting of the detector, high accuracy alignment jigs are used to ensure a precise alignment of the mechanics. The sensor ladders are all measured before mounting with a precision of a few μm using an optical measuring device and finally the whole detector is surveyed by a high precision probing machine measuring the position of points and surfaces in space. All this information is merged into a survey database describing the position of each strip on the sensors with a precision of $25\ \mu\text{m}$. The final geometrical database has to be obtained by software alignment using particle tracks in order to achieve the optimal resolution and also since the detector might have been distorted during transportation to DELPHI and installation into DELPHI. Particle tracks are also used to detect any movement of the detector inside DELPHI during the data taking period.

5 Software Development for the Vertex Detector

A crucial part of the work on the software is the alignment by which the exact position and direction of each sensor plane is determined. The starting point is the survey database and the silicon ladders are assumed to be rigid bodies. The existence of a third layer is useful in the alignment since the residual for a cluster with respect to a particle track can be determined by fixing the particle track using the two other layers. The complicated procedure of alignment is described in Ref. [93] and many effects have to be taken into account during the procedure. In brief, the alignment proceeds as follows: the outermost layer is first internally aligned using the areas, where neighbouring ladders overlap (“overlaps”); afterwards the individual ladders of the two other layers are aligned with respect to the corresponding ladders in the outermost layer and finally the whole detector is aligned with the rest of the DELPHI tracking system. In the alignment, mostly muons from Z^0 decays are used, but for the study of effects where high statistics is necessary, this sample is complemented by hadronic tracks from Z^0 decays.

5.1 Cluster Reconstruction Issues

In order to have the optimal resolution, it is important to use the charge information from the strips in the best way to determine the cluster position. Therefore, different cluster algorithms have been studied with the DELPHI sensors using both beam test data [94] and overlap residuals in DELPHI data [95] in order to find the optimum for each type of clusters. Furthermore, the charge should not be spread over too many strips, as already discussed above. This has been solved in DELPHI by enlarging the spacing between the strips on the Rz measuring n-side, wherever large incidence angles are expected so that the expected cluster width never exceeds five strips. On the $R\phi$ measuring p-side, the best algorithm to determine the cluster position was found to be the so-called η -algorithm. In the η -algorithm, the cluster position is reconstructed by

an interpolation of the two highest consecutive pulse heights (PH) of the cluster, and correcting for the non linear charge sharing evaluated from

$$\eta = \frac{PH_R}{PH_L + PH_R}, \quad (38)$$

where the subscripts L and R indicates the left and right strip. This algorithm is also suitable for the n-side, if the incidence angles are small enough so that the expected cluster width is not more than two strips.

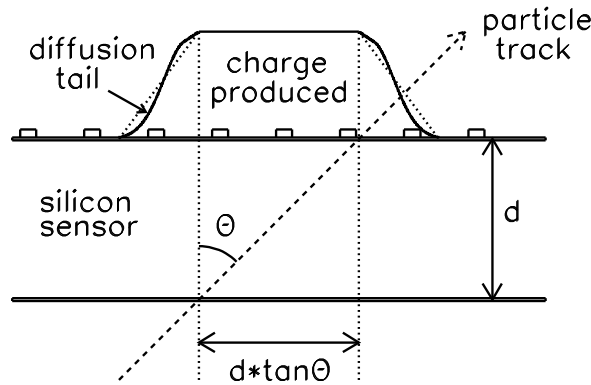


Figure 11: The ideal pulse shape of the cluster shape fitting algorithm [95]. θ is the incidence angle of the particle and d is the thickness of the sensor.

For large incidence angles, the distance traversed by the particles in the sensor plane is sufficiently large that most of the information is contained in the strips at the cluster edges. For such clusters, a special cluster shape fitting algorithm [95] was developed, in which the cluster position is determined by minimizing the difference between the measured and the predicted strip pulse heights using a χ^2 function. The pulse heights are predicted using an ideal pulse shape, shown in Figure 11, where the width of the diffusion tails are assumed to be constant and triangular in shape. In order to get the expected total pulse height, the total pulse height for particles with normal incidence was extracted from the data for each sensor type, assuming that the charge produced is linearly proportional to the path length in silicon. This algorithm improved the resolution considerably for intermediate incidence angles, where the difference between the observed resolution in DELPHI and the predicted resolution from the beam test data was largest.

The cluster positions with their errors are used together with track elements from other tracking detectors with their errors in the particle track fit in order to obtain the track parameters. The track fit gives as a result a track χ^2 per degrees of freedom (d.f.), describing the goodness of the track fit. The track $\chi^2/\text{d.f.}$ should be large, if the associated combination of clusters and track elements is not the correct one, but it might also become large if the assigned errors are not correct. Therefore, a good parameterization of the cluster errors is important. The high $\chi^2/\text{d.f.}$ of a particle track also tends to propagate into the χ^2 of any vertex the particle is assigned to, and hence complicate, the acceptance or the rejection of particles to vertices.

The precision by which a cluster determines the particle position depends, among other things, on the amount of charge produced, on the particle impact point in the silicon and on the track incidence angle with respect to the sensor plane, perpendicular to the direction of the strips. Therefore, the resolution was studied as a function of several variables in order to be able to assign the errors to the clusters reflecting more accurately the precision of the specific cluster. The studies were done using overlaps and particle tracks with clusters in all three layers. For $R\phi$ clusters, where the track incidence angles are generally small, the resolution mostly depends on the particle impact point and on the possibility that fast secondary electrons, delta-rays, were created along the particle path in silicon, which is reflected on the values of η and total pulse height, respectively. For Rz clusters, the resolution depends strongly on the track incidence angle, which is approximated to be similar to the polar angle of the particle direction. The dependence of the resolution on the variables mentioned above were used to parameterize the assigned errors, which are shown in Figure 12.

In order to test the validity of the error parameterizations, the distribution of the detector internal track $\chi^2/\text{d.f.}$ probability was calculated using particle tracks from $Z^0 \rightarrow \mu^+\mu^-$ events. The tracks were set by the innermost and outermost measured points and approximated as a circle (with a radius corresponding to measured transverse momentum) in $R\phi$ and as a straight line in Rz . The residual for the remaining associated clusters were calculated as the distance between this new track and the measured position of the cluster. The multiple scattering could be neglected, due to the high momenta of the particles. The track χ^2 was then defined as ratio between the sum

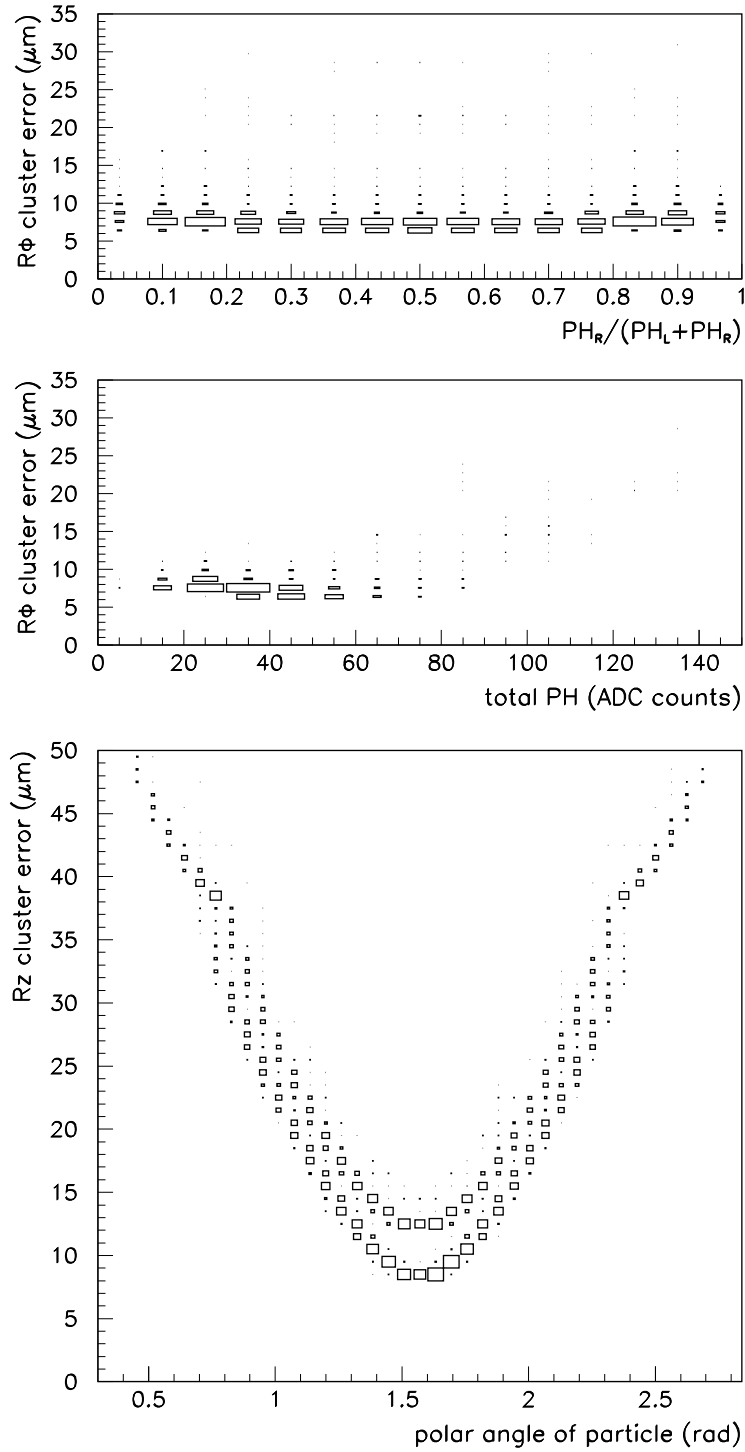


Figure 12: The assigned errors for $R\phi$ and Rz clusters as a function of the parameterization variables. In $R\phi$, only the two consecutive strips with highest pulse height (PH) are used. The subscripts L and R indicates the left and right strip of the two. The two distinguishable lines in the lowest plot are the parameterizations for the outermost layer (below) and the innermost layer (above).

of the squared residuals and the sum of the squared assigned errors. From the $\chi^2/\text{d.f.}$, a probability was then calculated for each particle track with at least three associated clusters. These probabilities are shown in Figure 13 for both $R\phi$ and Rz projections. This method is limited to the overlaps for the Rz projection since the detector only has two layers measuring the Rz coordinate. In both projections, the distribution has the characteristic flat shape with a peak at zero, mainly due to non-gaussian tails in the resolution function and badly reconstructed clusters.

Due to the complexity of the double sided sensors, it was also necessary to use sensors containing a small fraction of dead strips (i.e non sensitive to the signal) in DELPHI. Dead strips occur, for example, in sensors with so-called punch-throughs, which are pinholes in the insulating layer of the double metal structure on the n-side. These punch-throughs had been cured by removing the bond between the sensor and the electronic chip for the affected strips. Such an intervention degrades the precision but keeps the sensor efficient since the charge deposited on an unconnected strip is collected by neighbouring strips. In the case of a particle traversing the sensor close to such a dead strip, a simple algorithm of cluster search with a constant signal-to-noise threshold finds two separate clusters. This effect of cluster splitting is more pronounced on the n-side since at large track incidence angles, clusters have widths up to 4-5 strips and hence the splitting probability is larger.

Apart from the dead strips, there are also some other causes of cluster splitting. A particle with a large incidence angle generates a signal on the n-side over several strips, giving rise to a wide cluster. In this case, the signal per strip is decreased in spite of the growth of the total produced charge. Thus, a fluctuation of the energy loss in silicon can result in the signal-to-noise for a strip being lower than the threshold and hence a split cluster. The specific design of the silicon sensors of the outermost layer also creates split clusters. Even and odd strips are shifted about 0.7 mm to accomodate the polysilicon bias resistors at the edge of the sensor, as shown in Figure 14. Particles passing close to the edges produce signal on every second strip. In addition, the multiplexing of the readout on the n-side causes split clusters. The neighbouring strips of a cluster can be read out by nonconsecutive channels of the electronics, if the cluster occurs in the border region of two multiplexing zones. This case is also shown in Figure 14.

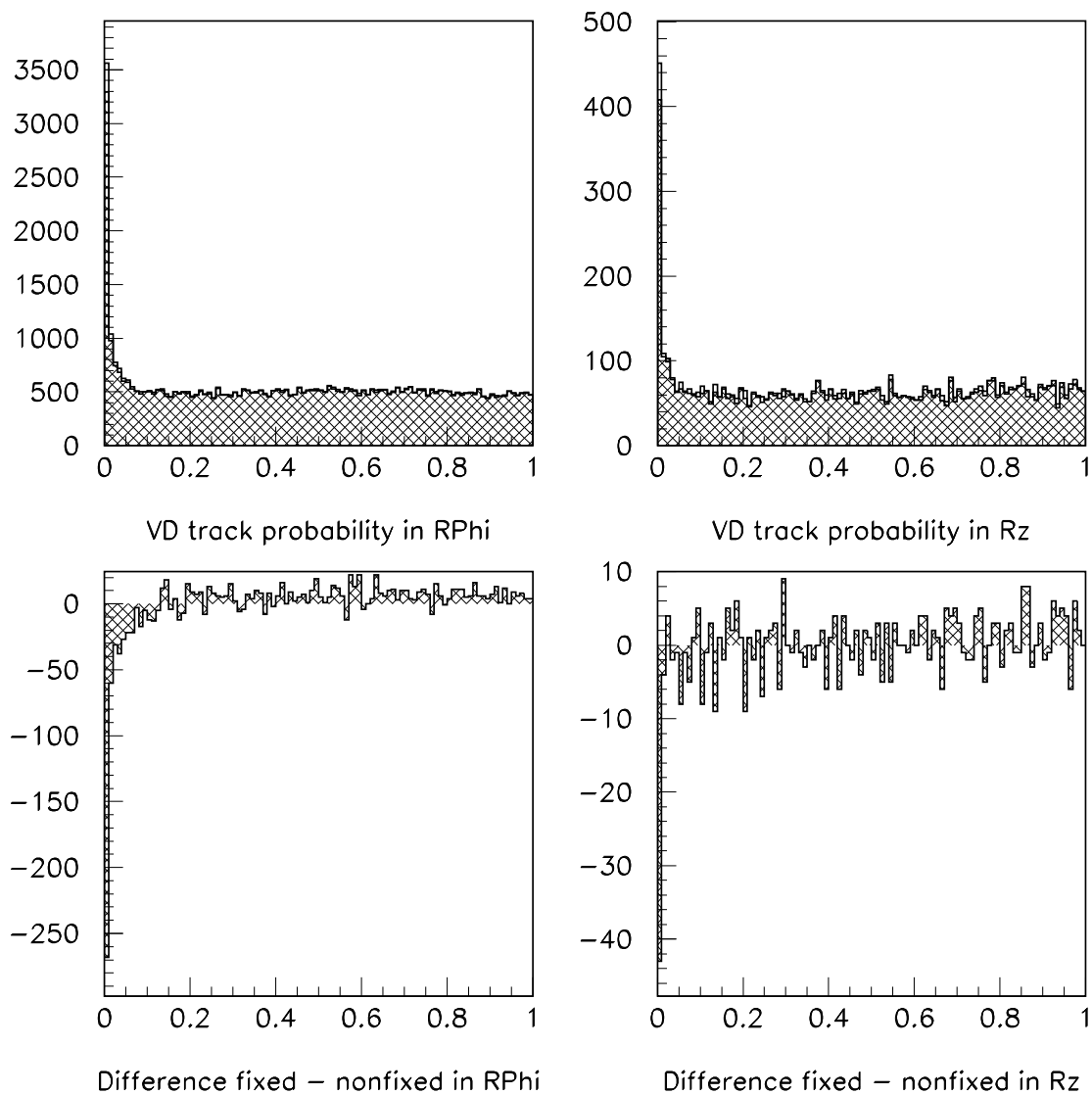


Figure 13: Internal $\chi^2/\text{d.f.}$ probability distributions for muon tracks from $Z^0 \rightarrow \mu^+\mu^-$ events with at least three associated clusters in the $R\phi$ plane (upper left) or the Rz plane (upper right). The effect of the cluster fixing procedure is made visible by subtracting the fixed and non-fixed distributions from each other. For the difference (the hatched area) in $R\phi$ (lower left) a clear migration of tracks from very low probability to higher probabilities due to the fixing is seen. A similar effect can also be noticed for Rz (lower right) with less statistical significance.

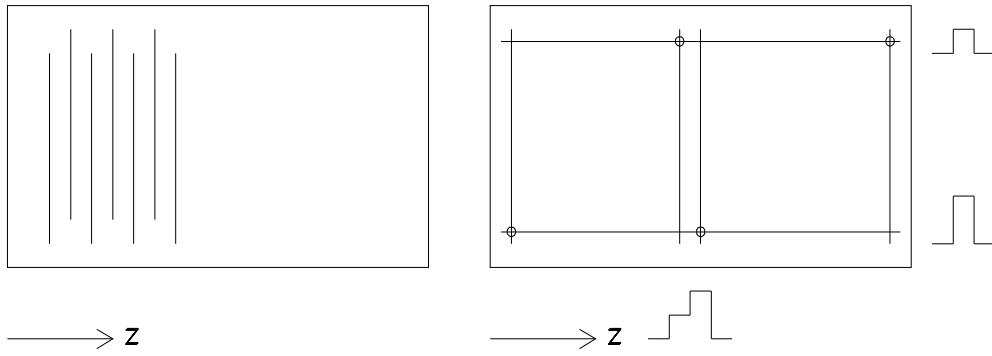


Figure 14: Left drawing: The design of the n-side of the sensors used for the outermost layer. Even and odd strips are shifted about 0.7 mm orthogonal to the z direction. Particles passing at the edges produce signals at every second strip. Right drawing: The multiplexing causes split clusters. The neighbouring strips of a cluster can be read out by electronic channels, which are not adjacent, if the cluster occurs in the region between two zones of the multiplexing on the n-side.

Due to these cluster splitting phenomena, a cluster fixing procedure was developed in order to recover the original clusters and assign correct errors to them [96]. The decision, whether a pair of adjacent clusters was a split cluster or not, was made based on the expected cluster size and the knowledge of the dead strips. The fraction of dead strips was 5 % and about 1 % of all reconstructed clusters were merged. The residuals of the merged clusters were studied and improvements were seen [96]. In Figure 13, the improvement due to the cluster fixing procedure can be seen as a migration of particle tracks to higher internal $\chi^2/\text{d.f.}$ probabilities. About 10 % of the particle tracks with low $\chi^2/\text{d.f.}$ probabilities are recovered by the procedure.

5.2 Improving Simulation Description

In simulations of detectors containing silicon microstrip sensors such as the DELPHI VD [97], the particles are followed in small steps through the silicon, generating electron-hole pairs according to the energy loss in silicon and generating secondary interactions such as delta-rays according to their probabilities. Afterwards, the electrons and the holes are allowed to drift in the electric field of the sensor adding the Lorentz drift due to the external solenoidal magnetic field. Comparing the simulation

and the data, it can be noticed that they differ mainly on two aspects, efficiency and resolution. The former is mainly due to the small percentage of sensors with defects or malfunctions, which make the efficiency dependent on the azimuthal angle and time. The latter is due to lack of knowledge of the exact position of each sensor and irregularities in shape and depletion. The DELPHI VD simulation has been improved in these aspects by methods commonly called “efficiency tables” and “shaken database”.

5.2.1 Efficiency Tables

An efficiency correction of the simulation is not dependent on the absolute efficiencies, but rather dependent on the ratio of the efficiencies in the data and simulation. Therefore, this ratio was determined in the efficiency table procedure [98] for each electronic readout chip, of which there are either three, four or five on a sensor. The ratio was determined using the associated clusters of well measured particles within the VD acceptance. This way qualitative differences between the data and the simulation have less significance on the ratio. Also, time dependencies were studied and ratios were determined separately for different run periods, if clear time dependencies of the efficiency for certain chips were noticed. In such cases, several efficiency tables were made corresponding to different run periods.

In simulated events, each reconstructed cluster could be removed with a probability equal to one minus the efficiency ratio of the corresponding chip. If the ratio was larger than one, i.e. the data was more efficient than the simulation, no cluster was removed from such a chip. When time dependencies were discovered in the data, the efficiency table used for a simulated event was selected based on probabilities proportional to the fraction of events contained in each period. In this way, not only the average efficiency was described but events were generated both with a higher and a lower efficiency when the chip efficiency changed dramatically during a data taking year. Azimuthal angle dependencies and time dependencies of the efficiency are of importance for measurements such as R_b , the partial decay width of $Z^0 \rightarrow b\bar{b}$ [99], since they lead to time and angular dependencies of the b selection efficiency and purity.

5.2.2 Shaken Database

In the software alignment, the position and direction of each sensor plane is determined using a subsample of all charged particles carefully selected for the purpose. However, due to the limited statistics, the fact that certain effects must be parameterized by averaging over a number of sensors and that the magnitude of certain effects is only known relative to another sensor, there are significant uncertainties in the exact description of the sensor planes. Moreover, it is known that the sensors are not completely flat and that different sensors have different depletion depths, leading to different distributions of the electron-hole pairs produced. All these effects cannot possibly be simulated, but instead the average could be described in terms of a change of the geometrical position and direction of each sensor plane with respect to the simulated one. An indication that the uncertainty in the knowledge of the exact positions and shapes of individual sensor planes is the cause of the degraded resolution, seen in large silicon sensor assemblies, is the fact that the resolution obtained with beam test data is generally significantly better than in more complicated structures, as can be observed, for example, by comparing the results in Ref. [2] and [94].

In DELPHI VD, a solution was chosen, in which each sensor was translated and rotated (“shaken”) for each simulated event so that the average resolution measured in the data was reproduced. The rotations were introduced to reduce any possible correlated systematics due to the fact that a large fraction of the particles contained in a quark jet, which is relatively narrow at LEP due to the boost, goes through the same sensor. The event-by-event shaking was done to reproduce the dispersion at sensor level and thereby avoided azimuthal angle dependencies, which are largely removed by the software alignment procedure for the data, in the simulation. The shaking was also done separately for the p- and n-side since they are decoupled in the software alignment using data, and the electrons and holes have different depletion depths.

Each sensor is uniquely defined in space by the position of the center of the sensor and a pair of vectors describing the sensor plane. It is customary in DELPHI to call these two vectors \vec{V} and \vec{W} , where \vec{V} is defined to be parallel to the implants and \vec{W} perpendicular to them as shown in Figure 15. In addition, a third vector called \vec{R} is usually defined to be orthogonal to the plane and pointing outward, seen from the

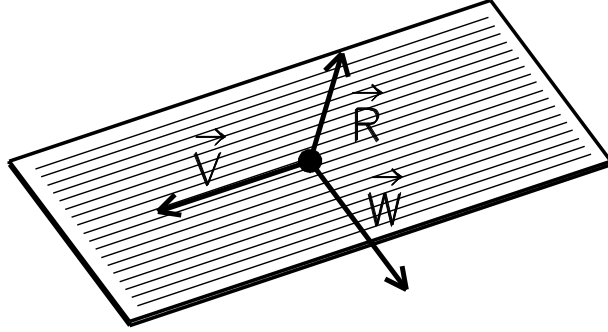


Figure 15: A sensor with the vectors defining the sensor plane for the p-side.

interaction point. The shaking is introduced by translating the position of the center of the sensor in R , $R\phi$ and z and rotating the vectors defining the plane according to (39). The angles are defined so that α is the rotation angle of the $\vec{V} - \vec{W}$ plane, β the rotation angle of the $\vec{V} - \vec{R}$ plane and γ the rotation angle of the $\vec{W} - \vec{R}$ plane.

$$\begin{pmatrix} \vec{V}' \\ \vec{W}' \\ \vec{R}' \end{pmatrix} = \begin{pmatrix} 1 & -\alpha & +\beta \\ +\alpha & 1 & -\gamma \\ -\beta & +\gamma & 1 \end{pmatrix} \begin{pmatrix} \vec{V} \\ \vec{W} \\ \vec{R} \end{pmatrix} \quad (39)$$

The translations and rotation angles are taken from a generated gaussian distribution with a width determined from a tuning procedure where the average resolution, as a function of the polar and azimuthal angles, is made to reproduce the measured data resolution. The tuning is different for each year since the resolution obtained in the data differs from year to year. This is a consequence of the extraction of the detector at the end of each data taking year and hence the software alignment has had to be redone. For the simulation to be compared with the 1995 data, for example, the widths of the translations obtained were $6.4 \mu\text{m}$ in $R\phi$, $7.3 \mu\text{m}$ in z , $20 \mu\text{m}$ and $37 \mu\text{m}$ in R for the p-side and the n-side, respectively. The widths for the rotations angles were 0.15 mrad for both β and γ on the p-side and 0.4 mrad for both β and γ on the n-side. The width of the α angle was set to zero since it is expected to be very small and should essentially be due to mask misalignments at the production stage of the sensors. Since the rotation angles are small, the rotation matrix can be approximated by the rotation matrix for infinitesimal rotations, and the rotation of the sensor plane

is then given by (39).

A comparison of the impact parameter distributions in data and simulation is shown in Figure 16 with the shaking procedure applied and a relatively comprehensive agreement on the full distribution can be seen. The quantity used in physics analysis is not the impact parameter but the impact parameter significance, which is the impact parameter divided by its error. For the impact parameter error, a tuning procedure [100] has been developed in order to fine tune the impact parameter errors to values closer to the observed ones and thereby obtain agreement between data and simulation on the significance. The fundamental changes in the track search and the improvements in the error parameterizations for the different tracking detectors have made the tuning easier and the amount of tuning necessary considerably smaller [100].

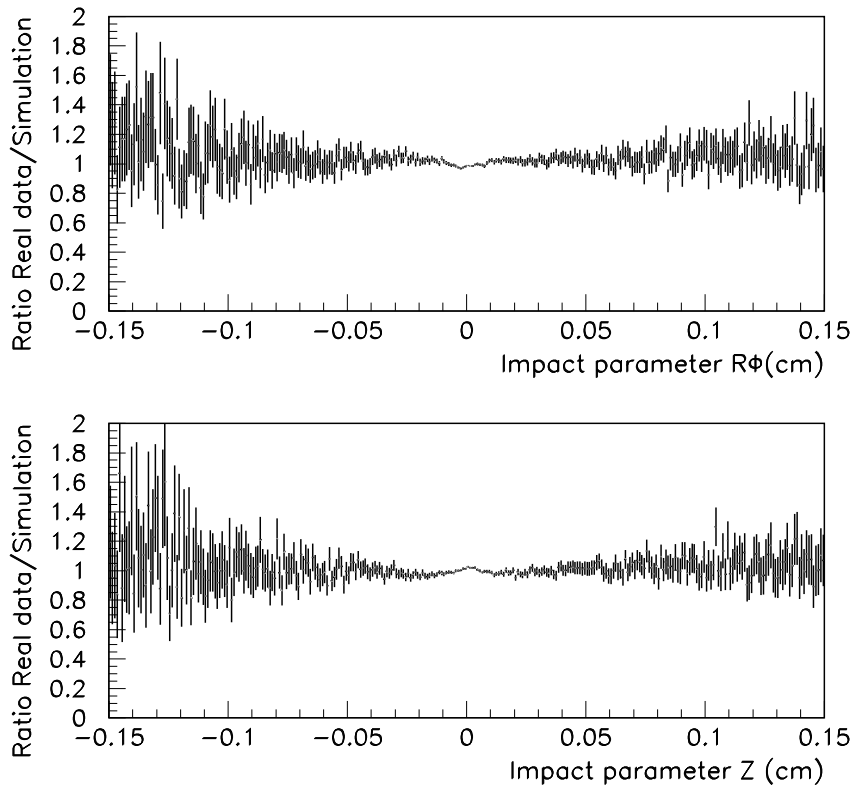


Figure 16: The ratio of the impact parameter distributions for particles from hadronic Z^0 decays in 1995 data and simulation. The distributions for data and simulation agree well even for large impact parameters.

6 Conclusions

The electroweak measurements from LEP have drastically improved the precision to which the free parameters of the Standard Model are measured so that many of the parameters by now have an experimental error of only one per mille or less. The measurements agree well with the model that is based on the spontaneously broken $SU(2)_L \otimes U(1)_Y \otimes SU(3)_C$ symmetry. The measurements have also significantly constrained the scenarios for possible new physics beyond the Standard Model. However, the origin of masses remains still to be explained, since no Higgs particle has yet been discovered and several theoretical arguments such as the large number of free parameters in the Standard Model suggest that a more fundamental theory should exist.

No definite sign of new physics has been found, neither for quarks nor for leptons. The universality of the $e-\mu-\tau$ coupling to charged and neutral currents has been verified to a few per mille level. No additional leptons have been discovered and the lepton family flavour is conserved at the level of currently achievable experimental precision. A large variety of searches and precision measurements are, however, currently performed at different particle colliders and new experiments are planned in order to discover the Higgs particle(s) and reveal information on the physics beyond the Standard Model.

A major breakthrough in particle detector technology over the last decade has been the development of silicon sensor production using a planar technology. These densely packed sensor elements allow high precision tracking, which enables studies of decay vertices of long lived particles such as B-hadrons. DELPHI has been one of the first collider experiments to install a silicon vertex detector and has put special emphasis on minimizing the material so that the high precision is retained also at lower momenta. The silicon vertex detectors will continue to play an important role in the upcoming LEP2 runs, since the neutral Higgs boson is expected mainly to decay into a $b\bar{b}$ -quark pair. To fully profit from the excellent position resolution and performance of the silicon sensors, a large effort has been made in DELPHI to understand the behaviour of the sensors and to develop software, in which this knowledge is optimally used.

References

- [1] N. Bingefors et al., *Nuclear Instruments & Methods* **A328** (1993) 447.
- [2] V. Chaubaud et al., *Nuclear Instruments & Methods* **A368** (1996) 314.
- [3] P. Chochula et al., DELPHI 97-121 CONF 103 (EPS-HEP 97 #306)(8 August 1997).
- [4] M. Battaglia, P. Kluit and K. Österberg, DELPHI 93-69 PHYS 296 (25 June 1993).
- [5] H. Videau, in *Proc. of the 28th International Conference on High Energy Physics*, eds. Z. Ajduk and A. K. Wroblewski (World Scientific, Singapore, 1997), p. 1013.
- [6] B. Heltsey, in *Proc. of the Third Workshop on Tau Lepton Physics*, ed. L. Rolandi, *Nuclear Physics* **B40** (1995) 413.
- [7] W. Hao, Ph.D. thesis, University of Leiden (1 February 1996).
- [8] R. Barate et al., *Eur. Phys. J.* **C1** (1998) 65.
- [9] S. Glashow, *Nucl. Phys.* **22** (1961) 579; S. Weinberg, *Phys. Rev. Lett.* **19** (1967) 1264; A. Salam, in *Proc. 8th Nobel Symposium*, ed. N. Svartholm (Almqvist and Wiksell, Stockholm, 1968), p. 367.
- [10] Y. Nambu, in *Preludes in Theoretical Physics in Honor of V. F. Weisskopf*, ed. A. De-Shalit, H. Feshbach and L. Van Hove (North-Holland, Amsterdam, 1966), p. 133; W. A. Baarden, H. Fritsch and M. Gell-Mann, in *Scale and Conformal Symmetry in Hadron Physics*, ed. R. Gatto (Wiley, New York, 1973) p. 139; H. Fritsch, M. Gell-Mann and H. Leytwyler, *Phys. Lett* **47B** (1973) 365; D. J. Gross and F. Wilczek, *Phys. Rev. Lett.* **30** (1973) 1343; H. D. Politzer, *Phys. Rev. Lett.* **30** (1973) 1346.
- [11] M. Chaichian and N. F. Nelipa, “Introduction to Gauge Field theories” (Springer, Berlin, 1984).
- [12] P. W. Higgs, *Phys. Lett* **12** (1964) 132; *Phys. Rev. Lett* **13** (1964) 508; F. Englert and R. Brout, *Phys. Rev. Lett.* **13** (1964) 321; G. S. Guralnik, C. R. Hagen and T. W. B. Kibble, *Phys. Rev. Lett.* **13** (1964) 585; T.W.B. Kibble, *Phys. Rev.* **155** (1967) 1554.
- [13] E. C. G. Sudarshan and R. E. Marshak, in *Proc. Padua Conference on Mesons and Recently Discovered Particles* (1957); R. P. Feynman and M. Gell-Mann, *Phys.*

- Rev. **109** (1958) 193; E. C. G. Sudarshan and R. E. Marshak, Phys. Rev **109** (1958) 1860.
- [14] H. P. Nilles, Phys. Rep. **110** (1984) 1; R. Arnowitt, A. Chamseddine and P. Nath, in *N = 1 Supergravity* (World Scientific, Singapore, 1984).
- [15] Particle Data Group, “Review of Particle Properties”, Phys. Rev. **D54** (1996) 1.
- [16] The LEP Collaborations, DELPHI 97-167 PHYS 743 (3 November 1997).
- [17] See ref. [15], p. 85, and references therein.
- [18] See ref. [15], p. 94, and references therein.
- [19] See *e.g.*, S. M. Bilenky, A. Bottino, C. Giunti and C. W. Kim, DFTT 2/96, Torino (2 February 1996).
- [20] L. Maiani, Phys. Lett. **B62** (1976) 183; L. Maiani in *Proc. of the 1977 International Symposium on Lepton and Photon Interactions at High Energies* (DESY, Hamburg, 1977), p. 867.
- [21] See ref. [15], p. 401, and references therein.
- [22] See ref. [15], p. 102, and references therein.
- [23] See ref. [15], p. 412 and p. 496, and references therein.
- [24] M.L. Perl et al., Phys. Rev. Lett. **35** (1975) 1489.
- [25] See ref. [15], p. 256, and references therein.
- [26] W. J. Marciano and A. Sirlin, Phys. Rev. Lett. **61** (1988) 1815.
- [27] Y. S. Tsai, Phys. Rev. **D4** (1971) 2821, *ibid* Phys. Rev. **D13** (1976) 771.
- [28] R. Decker and M. Finkemaier, Nucl. Phys. **B438** (1995) 17.
- [29] R. J. Sobie, in *Proc. of the Third Workshop on Tau Lepton Physics*, ed. L. Rolandi, Nuclear Physics **B40** (1995) 139.
- [30] R. Decker et. al., Zeit. Phys. **C58** (1993) 445.
- [31] M. Finkemaier and E. Mirkes, Zeit. Phys. **C69** (1996) 243; J. Kühn, E. Mirkes and J. Willibald, TTP97-53, Karlsruhe (December 1997).
- [32] S. Weinberg, Phys. Rev. Lett. **18** (1967) 507.

- [33] T. Das, V. S. Mathur and S. Okubo, *Phys. Rev. Lett* **18** (1967) 761.
- [34] H. Georgi and S. L. Glashow, *Phys. Rev. Lett.* **32** (1974) 438; H. Fritzsch and P. Minkowski, *Ann. Phys.* **93** (1975) 193.
- [35] See *e.g.*, T. Appelquist in *Proc. of the Mexican school of Particles and Fields*, (Mexico City, Dec 2-12, 1990), p. 1.
- [36] See *e.g.*, S. Weinberg, *Phys. Rev* **D19** (1979) 1277; L. Susskind, *Phys. Rev* **D20** (1979) 2619; E. Fahri and L. Susskind, *Phys. Rev* **D20** (1979) 3404; S. Dimopoulos and L. Susskind, *Nucl. Phys.* **B155** (1979) 237; E. J. Eichten and K. D. Lane, *Phys. Lett.* **B90** (1980) 125.
- [37] Y. Kubota et al., *Nuclear Instruments & Methods* **A320** (1992) 66.
- [38] P. H. Chankowksi, R. Hempfling and S. Pokorski, *Phys. Lett.* **B333** (1994) 403.
- [39] The LEP Collaborations, CERN-PPE/97-154 (2 December 1997).
- [40] R. Escribano and E. Masso, *Phys. Lett.* **B395** (1997) 369.
- [41] M. A. Samuel, G. Li and R. Mendel, *Phys. Rev. Lett.* **67** (1991) 668.
- [42] L. Silvestris, in *Proc. of the 28th International Conference on High Energy Physics*, eds. Z. Ajduk and A. K. Wroblewski (World Scientific, Singapore, 1997), p. 1219.
- [43] J. C. Pati and A. Salam, *Phys. Lett.* **B58** (1975) 333; R. N. Mohapatra and G. Senjanovic, *Phys. Rev. Lett.* **44** (1980) 912; J. Maalampi and K. Enqvist, *Phys. Lett.* **B97** (1980) 21; M. Gronau, C. N. Leung and J. L. Rosner, *Phys. Rev.* **D29** (1984) 2539; J. Bagger et al., *Nucl. Phys.* **B258** (1985) 565.
- [44] J. C. Pati and A. Salam, *Phys. Rev.* **D10** (1974) 275; R. N. Mohapatra and J. C. Pati, *Phys. Rev.* **D11** (1975) 566; R. N. Mohapatra and G. Senjanovic, *Phys. Rev.* **D12** (1975) 1502.
- [45] T. Yanagida in *Proc. of Workshop on the unified theory and baryon number in the Universe*, KEK-79-18 (1979); M. Gell-Mann, P. Ramond and R. Slansky, in *Supergravity*, eds. D. Z. Freedman and P. van Nieuwenhuizen, (North Holland, Amsterdam 1980) p. 315.
- [46] M. Dittmar, M. C. Gonzales-Garcia, A. Santamaria and J. W. F. Valle, *Nucl. Phys.* **B332** (1990) 1.

- [47] R. Barbieri, Rare Z decays in *Z physics at LEP1*, eds. G. Altarelli, R. Kleiss and C. Verzegnassi CERN 89-08, Vol.II (1989) p. 133.
- [48] P. Abreu et al., *Zeit. Phys.* **C74** (1997) 57.
- [49] C. Jarlskog, *Phys. Lett.* **B241** (1990) 579.
- [50] P. Depommier and C. Leroy, *Rep. Prog. Phys.* **58** (1995) 61.
- [51] S. Weinberg, *Phys. Rev.* **112** (1958) 1375.
- [52] W. J. Marciano, in *Proc. of the Third Workshop on Tau Lepton Physics*, ed. L. Rolandi, Nuclear Physics **B40** (1995) 3.
- [53] E. Glover and J. Van der Bij, Rare Z decays in *Z physics at LEP1*, eds. G. Altarelli, R. Kleiss and C. Verzegnassi CERN 89-08, Vol.II (1989) p. 34.
- [54] C. Martinez-Rivero, in *Proc. of the 28th International Conference on High Energy Physics*, eds. Z. Ajduk and A. K. Wroblewski (World Scientific, Singapore, 1997), p. 1456.
- [55] G. Eigen, in *Proc. of the Third Workshop on Tau Lepton Physics*, ed. L. Rolandi, Nuclear Physics **B40** (1995) 281; K. W. Edwards et al., *Phys. Rev.* **D55** (1997) 3919; G. Bonvicini et al., *Phys. Rev. Lett.* **79** (1997) 1221; D. W. Bliss et al., CLNS 97/1530, Cornell (8 December 1997).
- [56] U. Bellgardt et al., *Nucl. Phys.* **B299** (1988) 1; G. Bonvicini et al., *Phys. Rev. Lett.* **79** (1997) 1221.
- [57] M. Chaichian and K. Huitu, *Phys. Lett.* **B384** (1996) 157.
- [58] R. D. Bolton et al., *Phys. Rev.* **D38** (1988) 2077; K. W. Edwards et al., *Phys. Rev.* **D55** (1997) 3919.
- [59] R. Arnowitt and P. Nath, *Phys. Rev. Lett.* **66** (1991) 2708.
- [60] P. Abreu et al., *Phys. Lett.* **B359** (1995) 411.
- [61] A. Pich et al., *Phys. Lett.* **B196** (1987) 561.
- [62] S. Tisserant and T. N. Truong, *Phys. Lett.* **B115** (1982) 264; H. Neufeld and H. Rupertsberger, *Zeit. Phys.* **C68** (1995) 91.
- [63] D. Buskulic et al., *Zeit. Phys.* **C74** (1997) 263; J. Bartelt et al., *Phys. Rev. Lett.* **76** (1996) 4119.

- [64] B. A. Li, *Phys. Rev.* **D55** (1997) 1436.
- [65] LEP design report, CERN/LEP 84-01 (June 1984).
- [66] D. Decamp et al., *Nuclear Instruments & Methods* **A294** (1990) 121.
- [67] P. Aarnio et al., CERN/LEPC 83-3 (17 May 1983); P. Aarnio et al., *Nuclear Instruments & Methods* **A303** (1991) 233.
- [68] B. Adeva et al., *Nuclear Instruments & Methods* **A289** (1990) 35.
- [69] K. Ahmet et al., *Nuclear Instruments & Methods* **A305** (1991) 275.
- [70] P. Abreu et al., *Nuclear Instruments & Methods* **A378** (1996) 57.
- [71] F. Hartjes et al., *Nuclear Instruments & Methods* **A256** (1987) 55.
- [72] C. Brand et al., *Nuclear Instruments & Methods* **A283** (1989) 567.
- [73] A. Amery et al., *Nuclear Instruments & Methods* **A283** (1989) 502.
- [74] S. J. Alsvaag et al., DELPHI 94-157 CAL 120 (15 December 1994).
- [75] S. Almedhed et al., *Nuclear Instruments & Methods* **A305** (1991) 320.
- [76] H. Fischer et al., *Nuclear Instruments & Methods* **A265** (1988) 218.
- [77] G. Alekseev et al., *Nuclear Instruments & Methods* **A269** (1988) 652.
- [78] Fastbus-ESONE Committee, ESONE/FB 01 Doc. (1983).
- [79] The DELPHI collaboration, DELPHI 89-44 PROG 137 (17 May 1989).
- [80] J. Seguinot and T. Ypsilantis, *Nuclear Instruments & Methods* **142** (1977) 377.
- [81] E. Anassontzis et al., *Nuclear Instruments & Methods* **A323** (1992) 351.
- [82] W. Adam et al., *Nuclear Instruments & Methods* **A338** (1994) 284.
- [83] W. Adam et al., *Nuclear Instruments & Methods* **A360** (1995) 416.
- [84] P. Abreu et al., *Phys. Lett.* **B334** (1994) 435.
- [85] P. Abreu et al., *Zeit. Phys.* **C72** (1996) 207.
- [86] D. Buskulic et al., *Phys. Lett.* **B332** (1994) 209.

- [87] M. Battle et al., Phys. Rev. Letters **73** (1994) 1079.
- [88] M. Battaglia and P. M. Kluit, DELPHI 96-133 RICH 90 (16 September 1996).
- [89] D. Buskulic et al., Phys. Lett. **B349** (1995) 585; R. Barate et al., CERN-PPE/97-138 (20 October 1997); D. Cinabro et al., Phys. Rev. Letters **70** (1993) 3700; A. Galloni and R. McNulty, DELPHI 97-129 CONF 108 (EPS-HEP 97 #320) (14 August 1997); R. Akers et al., Zeit. Phys. **C65** (1995) 183; G. Alexander et al., Zeit. Phys. **C72** (1996) 231.
- [90] G. R. Lynch and O. I. Dahl, Nuclear Instruments & Methods **B58** (1991) 6.
- [91] J. Kemmer, Nuclear Instruments & Methods **176** (1980) 449.
- [92] M. Caccia et al., Nuclear Instruments & Methods **A260** (1987) 124.
- [93] V. Chabaud et al., DELPHI 95-177 MVX 10 (12 December 1995).
- [94] H. Dijkstra et al., DELPHI 94-50 TRACK 79 (6 October 1994).
- [95] P. Mattsson, DELPHI 95-147 MVX 6 (18 September 1995).
- [96] A. Nomerotski, I. Stavitski and K. Österberg, DELPHI 96-134 MVX 17 (2 September 1996).
- [97] M. Caccia and A. Zalewska, DELPHI 91-80 MVX 2 (20 August 1991); M. Caccia et al., DELPHI 91-34 PROG 172 (5 June 1991).
- [98] M. Karlsson and G. C. Zucchelli, DELPHI 95-51 MVX 5 (15 May 1995).
- [99] G. J. Barker et al., DELPHI 97-106 CONF 88 (EPS-HEP 97 #419) (13 August 1997).
- [100] G. Borisov and C. Mariotti, Nuclear Instruments & Methods **A372** (1996) 181; G. Borisov and C. Mariotti, DELPHI 97-95 PHYS 717 (23 July 1997).